

Scalings and decay of fractal-generated turbulence

D. Hurst

Turbulence, Mixing and Flow Control Group, Department of Aeronautics, Imperial College London, London SW7 2BY, United Kingdom

J. C. Vassilicos

Turbulence, Mixing and Flow Control Group, Department of Aeronautics and Institute for Mathematical Sciences, Imperial College London, London SW7 2BY, United Kingdom

(Received 13 April 2006; accepted 21 December 2006; published online 13 March 2007)

A total of 21 planar fractal grids pertaining to three different fractal families have been used in two different wind tunnels to generate turbulence. The resulting turbulent flows have been studied using hot wire anemometry. Irrespective of fractal family, the fractal-generated turbulent flows and their homogeneity, isotropy, and decay properties are strongly dependent on the fractal dimension $D_f \leq 2$ of the grid, its effective mesh size M_{eff} (which we introduce and define) and its ratio t_r of largest to smallest bar thicknesses, $t_r = t_{\text{max}}/t_{\text{min}}$. With relatively small blockage ratios, as low as $\sigma = 25\%$, the fractal grids generate turbulent flows with higher turbulence intensities and Reynolds numbers than can be achieved with higher blockage ratio classical grids in similar wind tunnels and wind speeds U . The scalings and decay of the turbulence intensity u'/U in the x direction along the tunnel's center line are as follows (in terms of the normalized pressure drop $C_{\Delta P}$ and with similar results for v'/U and w'/U): (i) for fractal cross grids ($D_f = 2$), $(u'/U)^2 = t_r^2 C_{\Delta P} fct(x/M_{\text{eff}})$; (ii) for fractal I grids, $(u'/U)^2 = t_r (T/L_{\text{max}})^2 C_{\Delta P} fct(x/M_{\text{eff}})$, where T is the tunnel width and L_{max} is the maximum bar length on the grid; (iii) for space-filling ($D_f = 2$) fractal square grids, the turbulence intensity builds up as the turbulence is convected downstream until a distance x_{peak} from the grid is reached where the turbulence intensity peaks and then decays exponentially, $u'^2 = u'_{\text{peak}}{}^2 \exp[-(x - x_{\text{peak}})/l_{\text{turb}}]$, where $u'_{\text{peak}}{}^2$ increases linearly with t_r , $x_{\text{peak}} \propto t_{\text{min}} T/L_{\text{min}}$ (L_{min} being the minimum bar length on the grid), and $l_{\text{turb}} \propto \lambda^2 U/\nu$ (ν being the kinematic viscosity of the air and λ being the Taylor microscale); λ remains approximately constant during decay at $x \gg x_{\text{peak}}$. The longitudinal and lateral integral length scales also remain approximately constant during decay at $x \gg x_{\text{peak}}$.

© 2007 American Institute of Physics. [DOI: 10.1063/1.2676448]

I. INTRODUCTION

Research activity on fractal-generated turbulence has been slowly building up over the past six years or so.¹⁻⁷ However, only two of these studies have contributed results from laboratory experiments on fractal-generated turbulence, and they both do so for wakes of three-dimensional fractal objects. Here we present wind tunnel measurements of turbulence generated by fractal grids placed at the entrance of the test section in the spirit of earlier seminal works that used "classical grids," i.e., regular rectangular arrays of bars, to generate the turbulence.⁸⁻¹⁰

Various valid motivations for the general study of fractal-generated turbulence have been given.^{1-4,7} The more immediate motivations in the present paper are three. First, there is the issue of how to create ideal experiments on turbulence with well controlled conditions and very high Reynolds numbers. Conditions are usually well controlled in the wind tunnel where classical grids produce homogeneous isotropic turbulence but only with very moderate Reynolds numbers. High Reynolds number turbulence can be obtained in field measurements but with very little control over the type (whether statistically stationary, homogeneous, isotropic, etc.) of the turbulence measured. This issue has already been addressed over the past 15 years for homogeneous iso-

tropic turbulence with some success (starting with Makita¹¹ and Mydlarski and Warhaft¹²) by replacing the classical grids with active ones in the wind tunnel. Here we try fractal grids in the wind tunnel. However, to preempt our conclusions, we cannot claim yet that we have been successful in designing the ideal turbulence experiment.

Our second and third motivations are the following two questions, and for these our findings are perhaps more interesting:

- (i) How does a turbulence decay when it is generated by creating many eddies of many different sizes at once, which is what a fractal grid is doing?
- (ii) How does a turbulence scale when it is generated by a fractal grid that has its own intrinsic scaling?

We report here an extensive exploratory study on fractal-generated turbulence. It is extensive because a total of 21 grids pertaining to three different fractal families and two different wind tunnels have been used. It is exploratory because what we present is a necessary first exploration into the broad landscape of properties and effects pertaining to fractal-generated turbulence. As a consequence, many of our experimental results may just be indicative and may call for further investigations on each and every single one of our grids if definite interpretations are to be reached. However,

the directions of such further investigations and some reasons for why they may be worthwhile are nevertheless clear in our conclusions.

The paper is structured as follows. Section II describes the experimental apparatus and Sec. III the three families of fractal grids used in this work and the quantitative ways to describe them. In Secs. IV–VI, we report our results on wind tunnel turbulence generated by fractal cross grids, fractal I grids, and fractal square grids, respectively. Each of these sections ends with a concluding subsection summarizing the main results for each family of grids. Overriding conclusions summarizing and comparing results obtained from all grids are given in Sec. VII.

II. EXPERIMENTAL APPARATUS

Experiments were conducted in two horizontal wind tunnels. One is a recirculating wind tunnel with a test section of $T^2=0.91^2 \text{ m}^2$ cross section and 4.8 m length. This tunnel was designed for turbulence research, so it has a low background turbulence level (measured to be 0.25%). When empty, the maximum speed in the tunnel is 45 m/s.

The other tunnel is a conventional open-circuit wind tunnel with a working section of $T^2=0.46^2 \text{ m}^2$ cross section and 3.6 m length. Its maximum speed, when empty, is 33 m/s and the background turbulence intensity is 0.4%.

Flow velocities were measured by hot wire anemometry. The hot wires used in this work were manufactured from wollaston wire consisting of a $5 \mu\text{m}$ diameter, platinum alloy core (10% rhodium) coated with silver up to an external diameter of 20–25 μm . The wires were soft-soldered to the top of a Dantec 55P51 x-wire probe. This probe has straight prongs with sensor angles of 45° and a 1 mm spacing between the two sets of prongs. The wire sensing element was then obtained by etching away a central portion of the silver coating in an electrolytic nitric acid bath. The resulting platinum element was roughly 1 mm long, giving a sensing length-to-diameter ratio of $l_w/d_w \approx 200$. A 6 mm diameter Dantec 55H24 probe support was used to support the x-wire probes.

In all our measurements, it was estimated that $l_w \approx 3 - 8\eta$, where η is the Kolmogorov length scale.

We used a state-of-the-art AALab AN-1005 constant-temperature anemometer system with four channels of which we used two. This anemometer has a high-frequency response (80 kHz using $5 \mu\text{m}$ wollaston wires) and enables accurate small-scale measurements to be made. The highest resolvable frequency is of order U/l_w , where U is the mean free-stream velocity. In both tunnels, U was varied between 6 and 20 m/s, which gives a maximum frequency of 20 kHz for our wires ($l_w \approx 1 \text{ mm}$), well within the capabilities of our anemometer.

The AALab anemometer has built-in signal conditioners, filters, and an acquisition card. The built-in signal conditioners were used to offset and amplify the analogue signals output by each anemometer. The resolution of the built-in acquisition card is 16 bit. A typically expected signal-to-noise ratio is 60 dB.



FIG. 1. The three fractal-generating patterns, $S=2, 3, 4$.

The hot wires were statically calibrated in the free-stream flow of the wind tunnels used in this testing. The free-stream velocity was measured using a 6 mm pitot-static probe, fixed at the inlet of the tunnel and connected to a Betz manometer. Homogeneity traverses were performed to verify that the local free-stream velocity matched the inlet velocity. Good calibrations are achieved with the AALab anemometer by fourth-order polynomial fits of the velocity as a function of voltage, which provides small corrections to the usual King's law.

Systematic directional calibrations of the x-wire were also performed, first by aligning it with the freestream flow to record anemometer voltage output at various tunnel speeds, then by setting the tunnel running at a constant speed and rotating the entire x-wire probe $\pm 20^\circ$ in 5° increments.

Sampling frequency was chosen so as to pick up the smallest scales accurately resolved by the anemometer/wire. To satisfy the Nyquist condition, sampling was carried out at twice the frequency of the smallest resolvable scales. Tunable low-pass filtering was used in order to remove noise and to prevent higher frequencies from folding back (aliasing) and distorting the lower frequencies of the sampled signal. The setting of the low-pass filter was always set to half the sampling frequency.

Data were sampled for a period of time that captured at least 100000 integral lengths of the flow. Such large samples are required to obtain accurate (converged) statistics, especially at large (infrequent) scales. A typical integral length was 5 cm, resulting in typical sampling times varying from 4 to 14 min.

III. THREE FAMILIES OF FRACTAL GRIDS

We considered three families of fractal grids each based on a different fractal-generating pattern (see Fig. 1).

These three patterns can be distinguished by the number S of rectangular bars they require, $S=2$ in the case of the cross, $S=3$ in the case of the I pattern, and $S=4$ in the case of the square. Fractal grids are completely characterized by the choice of pattern and (i) the number of fractal iterations N ; (ii) the bars' lengths $L_j = R_L^j L_0$ and thicknesses $t_j = R_t^j t_0$ (in the plane of the pattern, normal to the mean flow) at iteration j , $j=0, \dots, N-1$ (all these bars, irrespective of iteration and type of grid in this work, have the same 5 mm thickness in the direction of the mean flow, with the one exception of the grid of Fig. 13, which, unlike all other grids that are made of acrylic or wood, is made of steel and has a 1.6 mm thickness in the direction of the mean flow); (iii) the number B^j of patterns at iteration j .

$B=4$ and $R_L \leq 1/2$, $R_t \leq 1$ in all the fractal grids used here. By definition, $L_0 \equiv L_{\max}$, $L_{N-1} \equiv L_{\min}$, $t_0 \equiv t_{\max}$, t_{N-1}

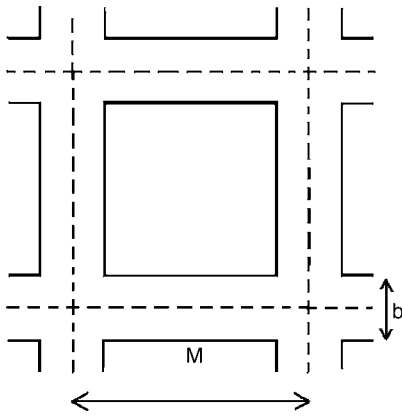


FIG. 2. Classical grid geometry.

$\equiv t_{\min}$. Scaled diagrams of all the fractal grids used in this investigation are shown in Figs. 3, 12, 13, 17, 32, and 33.

A. Derived quantities and parameters

The blockage ratio σ of these grids is the ratio of their total area to the area T^2 of the tunnel's cross section. A fractal grid's total area A is the sum of the areas A_j covered by each iteration j : $A_j = L_j t_j B^j$ and $A = S \sum_{j=0}^{N-1} A_j = S \sum_{j=0}^{N-1} L_0 t_0 (R_L R_t B)^j = S L_0 t_0 ([1 - (B R_L R_t)^N] / (1 - B R_L R_t))$. It follows that $\sigma = S (L_0 t_0 / T^2) ([1 - (B R_L R_t)^N] / (1 - B R_L R_t))$.

Scaling exponents β_L and β_t that characterize the area/blockage distribution across scales can be defined as follows: $A_j \sim L_j^{-\beta_L}$, $A_j \sim t_j^{-\beta_t}$. Higher/lower values of these β exponents mean that more/less of the blockage is to be found in the smaller scales of the grid. Note that, as a consequence of $A_j = L_j t_j B^j$, $L_j = R_L^j L_0$ and $t_j = R_t^j t_0$, $R_L^{\beta_L+1} R_t B = R_t^{\beta_t+1} R_L B = 1$, and $\sigma = S (L_0 t_0 / T^2) ((1 - R_L^{-\beta_L N}) / (1 - R_L)) = S (L_0 t_0 / T^2) ((1 - R_t^{-\beta_t N}) / (1 - R_t))$. The scaling exponent that characterizes the fractal perimeter, however, is a fractal dimension defined by $D_f = \log B / \log(1/R_L)$. Note that $1 \leq D_f \leq 2$.

It is also of interest to define the thickness ratio $t_r \equiv t_0 / t_{N-1} \equiv t_{\max} / t_{\min}$. Note that $t_r = R_t^{1-N}$.

Classical grids are a special case of our fractal grids where $S=2$; $\beta_t = \infty$ and $R_t = 1$; $R_L = 1/2$, $D_f = 2$; $\beta_L = 1$ and $t_r = 1$.

Unlike classical and even active grids, fractal grids do not have a well-defined mesh size. Intuitively it would make sense to define an effective mesh size M_{eff} as being proportional to the ratio of T^2 over the fractal perimeter's length P . However, such a definition does not take into account the blockage ratio σ because part of the tunnel's cross-sectional area is of course covered by the area of the grid. We calculate the σ correction to T^2/P by reference to classical grids as we want our definition of M_{eff} to return the mesh size M of classical grids when applied to them.

By direct inspection of Fig. 2 we see that in the case of a classical grid, $\sigma = \frac{b}{M} (2 - \frac{b}{M})$, where $b = t_j$ for all $j=0, \dots, N-1$ as $t_r = 1$. The perimeter of a single mesh being $4M(1 - \frac{b}{M})$ and there being a number $(T/M)^2$ of meshes in a classical grid, $P = (T/M)^2 4M(1 - \frac{b}{M})$. Hence we obtain two expressions for $\frac{b}{M}$ that equate to give $M = (4T^2/P) \sqrt{1 - \sigma}$.

We therefore define an effective mesh size for our fractal grids as follows:

$$M_{\text{eff}} = \frac{4T^2}{P} \sqrt{1 - \sigma}. \quad (1)$$

The fractality of the grids influences M_{eff} via their perimeter, which can be extremely long in spite of being constrained to fit within the area T^2 .

The simple requirement that the fractal grids must fit exactly into the tunnel's cross section implies that $T = L_{\max}$ in the case of cross grids but that $T = \sum_{j=0}^{N-1} L_j + t_{N-1} \approx L_{\max} [(1 - R_L^N) / (1 - R_L)]$ in the case of I and square grids.

A complete description of cross grids (assuming B is kept constant; here $B=4$) requires a minimum of four parameters, for example T , N , t_{\max} , and R_t , whereas a complete description of I and square grids (again assuming B is kept constant, here $B=4$ too) requires a minimum of five parameters, e.g., T , N , L_{\max} , t_{\max} , and t_{\min} . Note the extra constraint $R_L = 1/2$ (hence $D_f = 2$) in the case of cross grids.

B. The fractal grids

We constructed five different biplanar cross grids for the 0.912 m² wind tunnel, one of which is a classical grid. These grids differ by their thickness and blockage ratios. Three of the fractal cross grids have the same number of $N=4$ fractal iterations and very similar mesh sizes. Two of those have three identical parameters, T , N , and t_{\max} , and differ by their blockage ratio so as to allow comparisons at different blockage ratios while keeping all other independent parameters constant.

We also constructed for the 0.912 m² tunnel five different planar I grids, four of which have the same $t_{\min} = 1$ mm, $\sigma = 25\%$, and $N=6$ iterations. Thus, four of the five parameters required to completely determine these four fractal I grids (see Sec. III A) are fixed. The remaining parameter that we determine is the fractal dimension D_f , and we chose four values: $D_f = 1.68, 1.79, 1.87$, and 1.98 giving four different grids. These four grids have similar L_{\max} because L_{\max} turns out to be mostly constrained by the tunnel width. The purpose of these four grids is to determine the role of their fractal dimension at constant blockage ratio, minimum thickness, number of iterations, and tunnel size T . The purpose of the fifth I grid is to test dependencies on blockage and/or nondimensional parameters such as N , which is why it has $N=5$ (instead of $N=6$) iterations, $t_{\min} = 4$ mm, $D_f = 2.0$, and a higher blockage $\sigma = 31\%$ (which is made possible by the smaller number of iterations).

Following the results obtained from these fractal I grids, we designed and constructed five extra fractal I grids all with $D_f = 2$ for the purpose, as explained in the following sections, to maximize flow homogeneity. We kept $\sigma = 25\%$ as with the previous $N=6$ I grids. We designed these five new grids for the $T = 0.46$ m wind tunnel which, even though smaller, has effectively a longer test section (it is approximately 7.8 T long). To identify which length scale or length scales control turbulence decay, it is useful to construct fractal I grids with the same values of M_{eff} , σ , L_{\max} , and L_{\min} , for example, in which case we can establish the role of t_{\max} by varying it

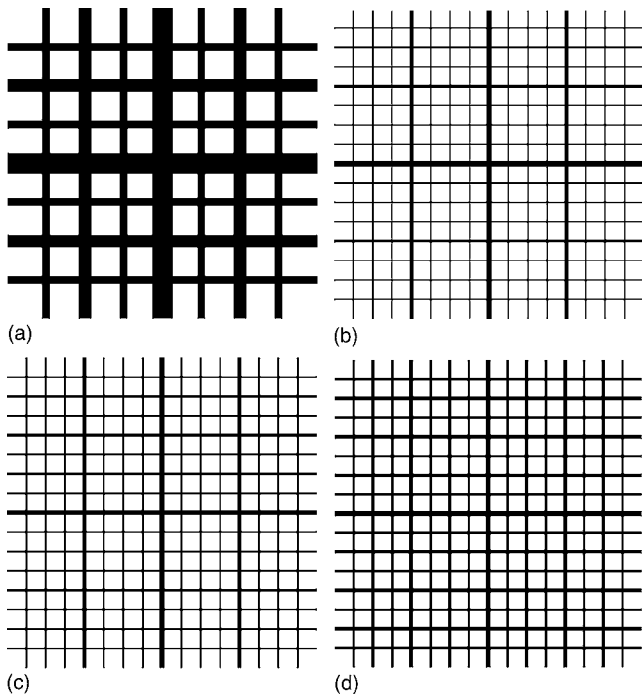


FIG. 3. The four nonclassical cross grids. From $t_r=R_L^{1-N}$, $R_L=0.55, 0.58, 0.71,$ and 0.79 from (a) to (d). (a) $t_r=3.3, t_{max}=62$ mm, $\beta_L=0.00, \sigma=40\%$; (b) $t_r=5.0, t_{max}=16$ mm, $\beta_L=0.18, \sigma=17\%$; (c) $t_r=2.8, t_{max}=14$ mm, $\beta_L=0.45, \sigma=21\%$; (d) $t_r=2.0, t_{max}=16$ mm, $\beta_L=0.58, \sigma=29\%$.

from grid to grid. We set $N=4$ and $M_{eff}=36$ or 37 mm for all these extra I grids. It is possible to widely vary t_r while only slightly varying M_{eff} within this narrow range because M_{eff} is predominantly controlled by R_L and N , which are both fixed to $1/2$ and 4 , respectively. Hence, the five extra grids differ by $t_r=2.5, 5.0, 8.5, 13.0,$ and 17.0 , but their lengths L_{max} and L_{min} turn out to be about constant for all five grids.

In an attempt to further improve flow homogeneity and isotropy, we then constructed for the $T=0.46$ m wind tunnel (test section's length ≈ 7.8 T) five different planar fractal square grids all with $D_f=2$ (space-filling) for best homogeneity, same $\sigma=25\%$ (which is also the blockage ratio of nine out of the ten I grids), $N=4$ (as for the space-filling I grids),

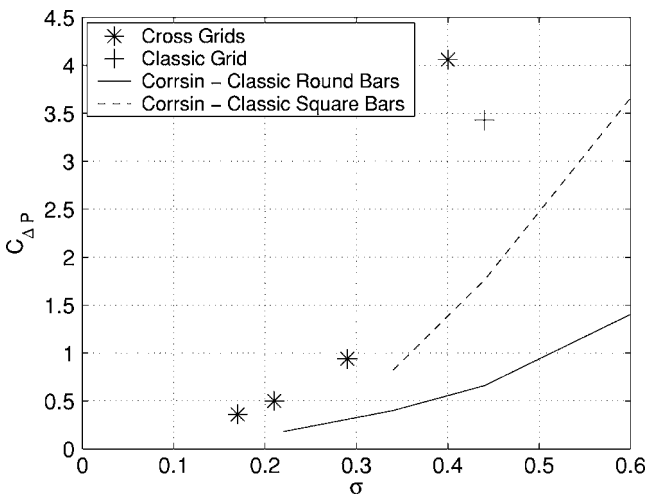


FIG. 4. $C_{\Delta P}$ vs grid σ .

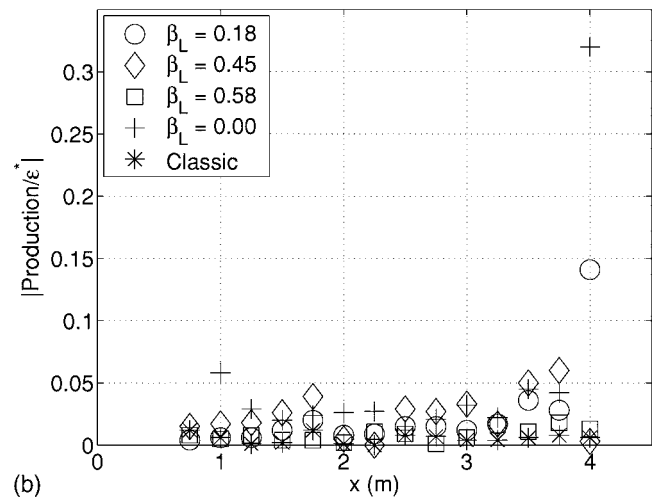
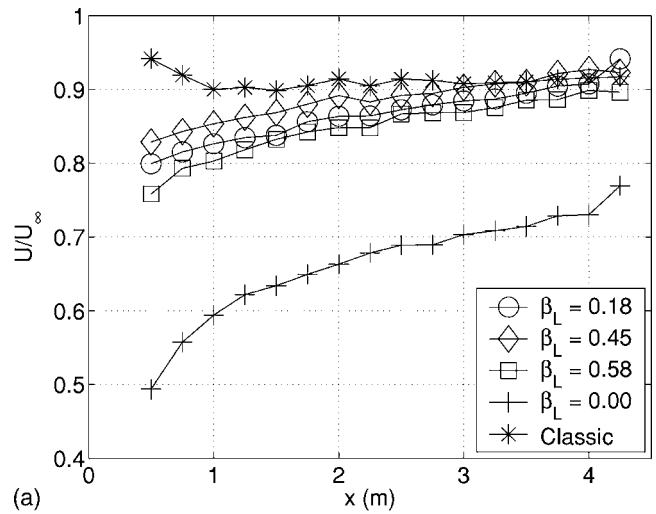


FIG. 5. Turbulence production, $T=0.91$ m tunnel, $U_{\infty}=12$ m/s. See Fig. 3 for grid correspondence with β_L .

and $M_{eff} \approx 26.5$ mm for all grids. It is possible to widely vary t_r while only slightly varying M_{eff} within a narrow range. The five space-filling square grids therefore differ by their values of t_r , and we chose the same five values of t_r , as for the five space-filling I grids: $t_r=2.5, 5.0, 8.5, 13.0,$ and 17.0 . By square construction and tunnel width constraint, $L_{max}=237.4$ mm and $L_{min}=29.7$ mm for all five grids.

The purpose of these five grids is to make a start toward identifying which length scale or length scales control turbulence decay. In this particular case, we have kept $M_{eff}, \sigma, L_{max},$ and L_{min} constant while varying only t_{max} and t_{min} from grid to grid.

For the purpose of investigating the effects of the wind tunnel width T , we constructed two space-filling fractal square grids with similar specifications as the five previous square grids but larger so as to fit into the test section of the $T=0.91$ wind tunnel (test section's length ≈ 5.25 T). For both of these larger square grids, $D_f=2.0, \sigma \approx 25\%, N=4,$ and the value of M_{eff} is very close to that of the five smaller square grids. It is again possible to widely vary t_r while only

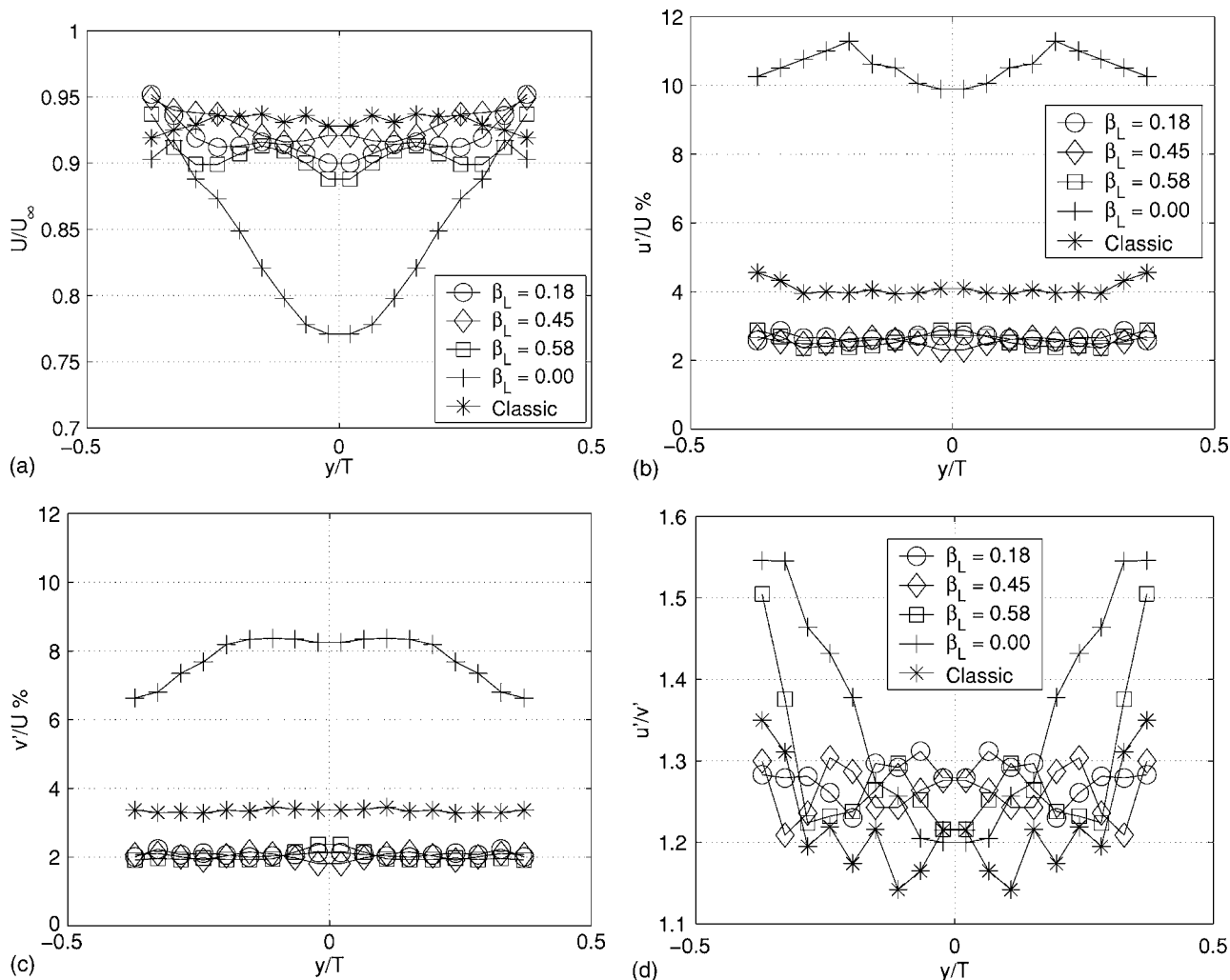


FIG. 6. Homogeneity profiles, $T=0.91$ m tunnel, $x=4.25$ m, $U_\infty=12$ m/s. See Fig. 3 for grid correspondence with β_L .

slightly varying M_{eff} within a narrow range. Hence, the two grids differ by their values of t_r : $t_r=17.0$ and 28.0 . L_{max} and L_{min} are about the same for both grids.

A complete quantitative description of all these fractal grids as well as fairly faithful pictorial descriptions of them are to be found in the following sections.

IV. TURBULENCE GENERATED BY FRACTAL CROSS GRIDS

We constructed five different biplanar cross grids for the 0.91^2 m² wind tunnel, one of which is a classical grid with $\sigma=44\%$, $M=152$ mm, $b=39$ mm. As shown in Fig. 3, these grids are distinguished by their thickness ratios, the classical grid (not shown in the figure) corresponding to $t_r=1$. They also have different blockage ratios that are given in the figure captions. The effective mesh size and N are $M_{\text{eff}}=114$ mm and $N=3$ for Fig. 3(a), but $N=4$ for the other three Figs. 3(b)–3(d), and the mesh sizes are, respectively, $M_{\text{eff}}=58.4$, 57, and 54 mm.

A. Pressure drop

The difference in pressure (ΔP) across each grid was measured using a Betz manometer for various mean flow

velocities U_∞ upstream of the grid. In agreement with classical measurements,⁹ it was found that $\Delta P \propto U_\infty^2$ thus defining a dimensionless normalized static pressure drop

$$C_{\Delta P} = \frac{\Delta P}{\frac{1}{2}\rho U_\infty^2}, \quad (2)$$

where ρ is the atmospheric air density.

It is shown in Sec. III that fractal cross grids only require four parameters to be completely described, and the four cross grids used here all have the same value of T ; three of these grids also have the same value of N [Figs. 3(b)–3(d)]; finally two of these three grids also have the same value of t_{max} [Figs. 3(b) and 3(d)]. Hence, specifying the blockage ratio σ determines completely these last two grids and Fig. 4 shows that increasing σ by 70% (from $\sigma=17\%$ to 29%) while keeping t_{max} , T , and N constant causes the pressure drop to more than double. Note that the bar aspect ratios, i.e., the ratios of bar thicknesses t_j to the bar thickness in the direction of the mean flow (which is 5 mm for all bars), change when σ changes while keeping T , N , and t_{max}

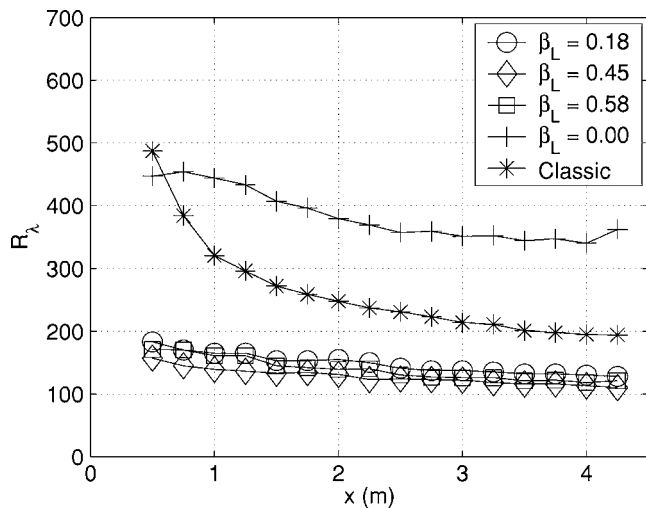


FIG. 7. Re_x as function of x measured in meters from the cross grids. $T = 0.91$ m tunnel, $U_\infty = 12$ m/s. See Fig. 3 for grid correspondence with β_L .

constant because of the fractal construction constraints detailed in Sec. III.

The increase of pressure drop with blockage ratio is confirmed by the other two cross grids [Figs. 3(a) and 3(c)] even though other independent parameters have also been

varied in their definition (including the bar aspect ratios), thus limiting the ability to firmly conclude as to the effect of σ .

Figure 4 also shows that $C_{\Delta P}$ is larger for our fractal cross grids than for classical grids at equal blockage ratio σ (extrapolating lines from Corrsin⁹ in that figure). The data point at $\sigma = 44\%$ is for our own classical grid and shows that $C_{\Delta P}$ is smaller than for fractal cross grids but higher than Corrsin's classical grids, which were made of circular or square cross-section bars. (Our classical grid also has square cross-section bars, but $T/M = 6$, whereas Corrsin's grids in Fig. 4 are such that $T/M = 40$. In fact, Corrsin⁹ always used $T/M = 20$ or 40 for best homogeneity and isotropy. The value of $C_{\Delta P}$ is notoriously sensitive to bar shape but even to T/M , at least where T/M is not large enough. The value of T/M_{eff} of our cross grids is 16 for all of them except for the one with the largest value of M_{eff} , for which $T/M_{\text{eff}} = 8$.) Designing grids that can generate as high $C_{\Delta P}$ as possible for a given σ is potentially interesting for various applications, but in particular for generating high Reynolds number turbulence in the wind tunnel (high $C_{\Delta P}$ causes high turbulence intensity) without the effort and complexity involved with active grids.^{11,12}

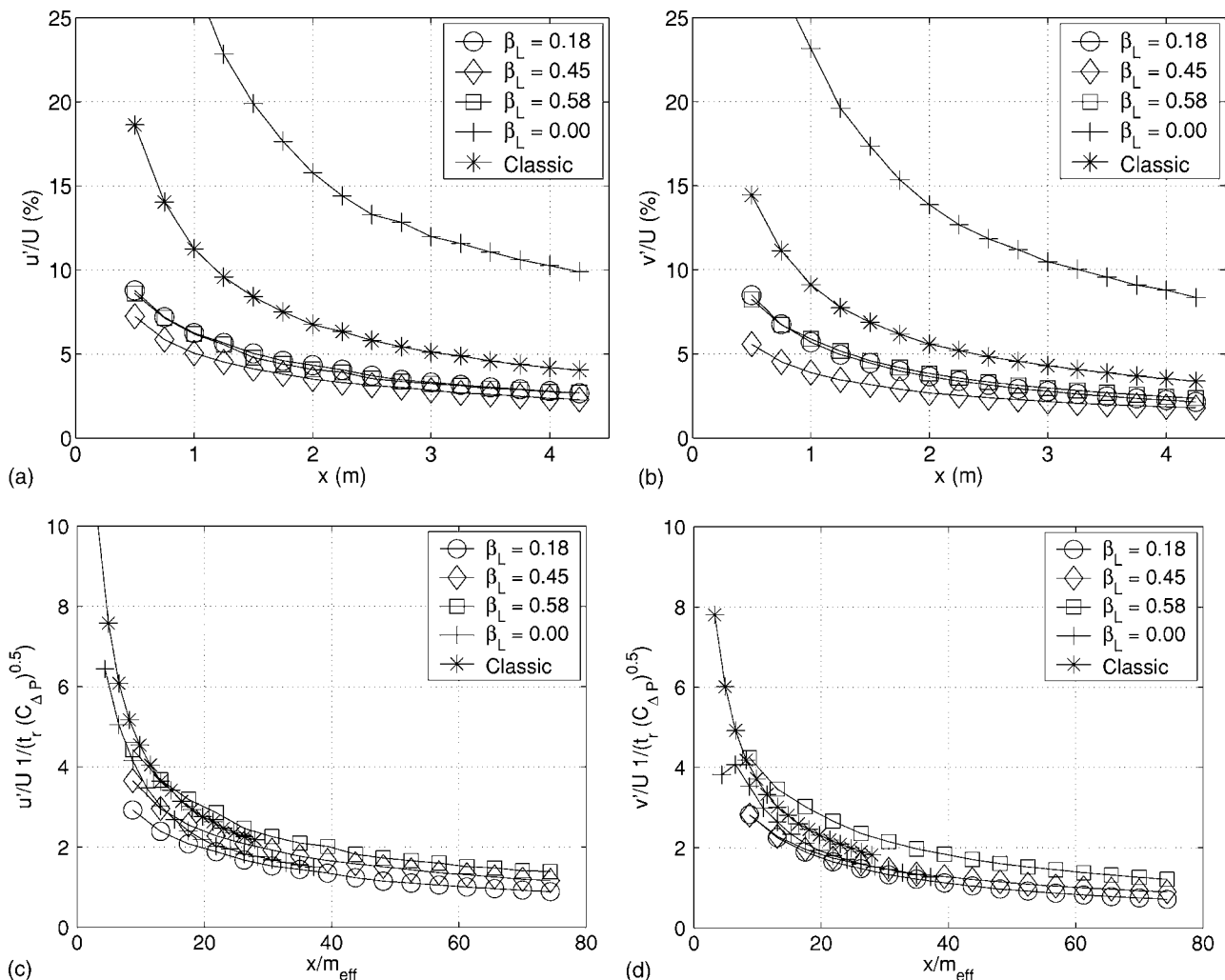
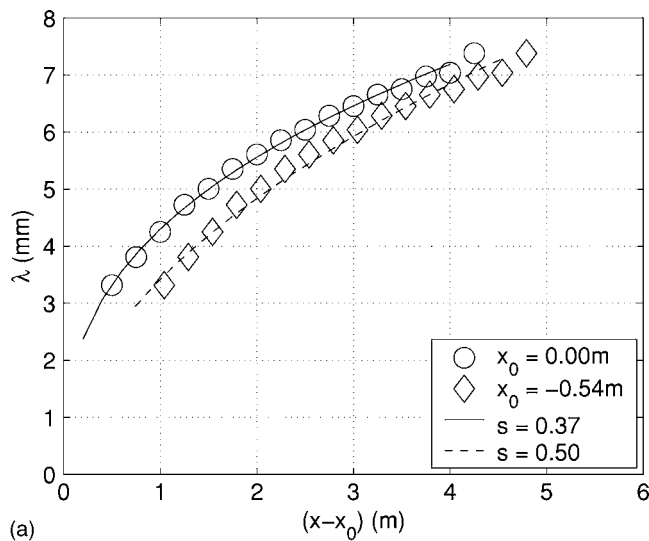
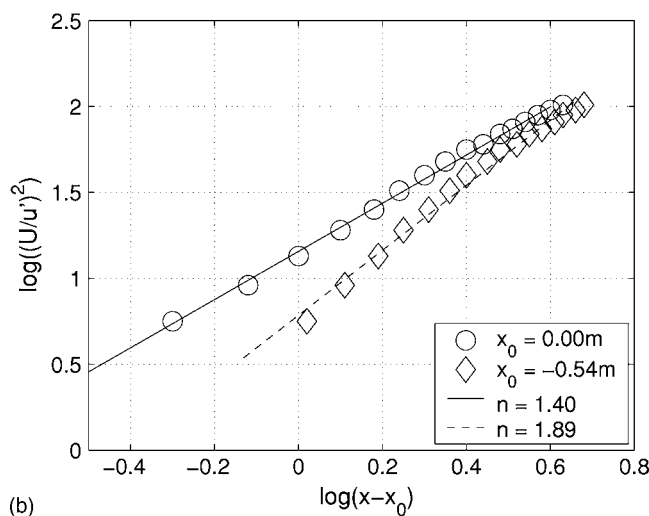


FIG. 8. Turbulence decay, cross grids, $T = 0.91$ m tunnel, $U_\infty = 12$ m/s. See Fig. 3 for grid correspondence with β_L .



(a)



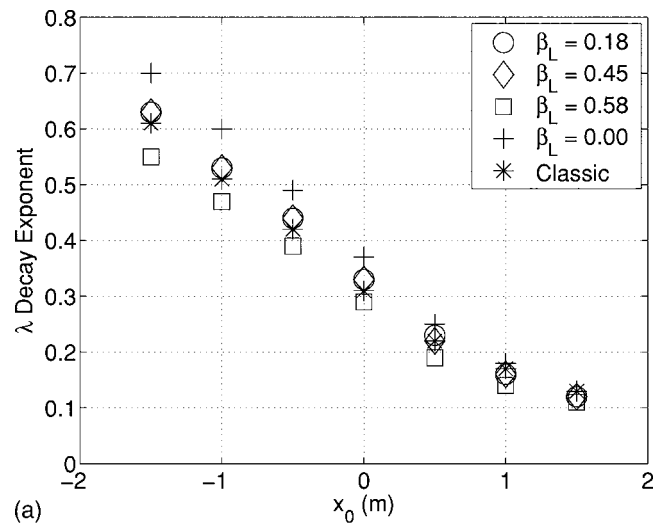
(b)

FIG. 9. Cross grid with $\sigma=40\%$, $T=0.91$ m tunnel, $U_\infty=12$ m/s.

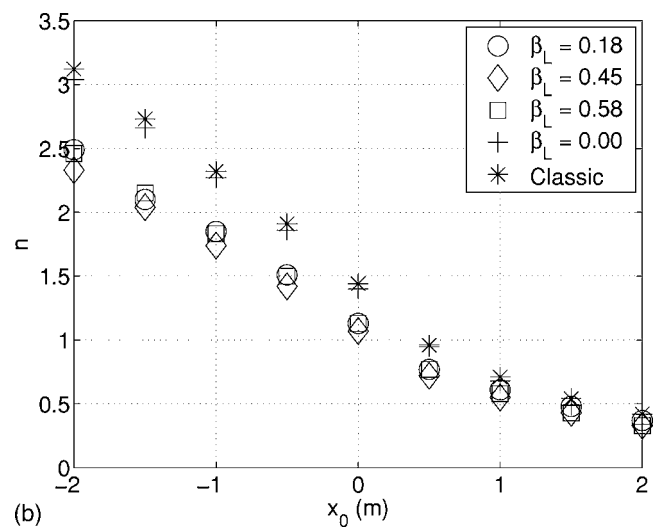
B. Turbulence production, homogeneity, and isotropy

Fractal cross grids generate nonzero values of $\frac{\partial U}{\partial x}$ on the tunnel's centerline near the grids (U is the mean flow velocity in the direction of the tunnel's central x axis) whereas classical grids do not (see Fig. 5). This longitudinal gradient causes some turbulence production $\mathcal{P} = -(u'^2 - v'^2) \frac{dU}{dx}$ (this formula, where u' and v' are the rms. longitudinal and lateral horizontal turbulence velocities, is valid on the center line for symmetric grids with respect to a 90° rotation¹³ such as cross and square grids but not I grids; the correction $v'^2 \frac{dU}{dx}$ comes from incompressibility,¹³ which implies longitudinal mean velocity gradients in the y and/or z directions too), which is, nevertheless, usually limited to within 5% of energy dissipation and often less, as shown in Fig. 5. The measure of dissipation used in this figure is ϵ^* obtained from $\frac{1}{2} U \frac{d}{dx} (u'^2 + v'^2 + w'^2) = \mathcal{P} - \epsilon^*$, where w' is the rms vertical turbulence velocity.

Gradients of U along x have to be offset by lateral gradients of U , for example along the horizontal y axis, which is orthogonal to the x axis and to the vertical z axis. Far enough from the grid, however, there seem to be no longitudinal



(a)



(b)

FIG. 10. Exponents s and n as functions of x_0 , $T=0.91$ m tunnel, $U_\infty=12$ m/s. See Fig. 3 for grid correspondence with β_L .

gradients of U and we might expect to find no lateral gradients of U either (inklings for how far it is to be far enough from the grid are given in the next paragraph). Due to time constraints and the large number of novel grids that have been tested in this work, it was not possible to produce comprehensive three-component velocity maps of the region around the tunnel centerline at many downstream locations for each grid. We only obtained lateral mean velocity profiles as far downstream as possible from the grid ($x=4.25$ m in the 0.91^2 m² wind tunnel) in order to quickly identify grids that do not produce homogeneous turbulence. In the case of cross grids, y profiles suffice because of their y - z symmetry. We plot them in Fig. 6 and comment on them in the following three paragraphs.

There is good U homogeneity for the three cross grids with relatively small effective mesh size [M_{eff} between 5.5 and 6.0 cm, i.e., say $M_{\text{eff}} \approx 57$ mm for all these three grids, see Figs. 3(b)–3(d)], but the cross grid with $M_{\text{eff}}=114$ mm [Fig. 3(a)] generates a significant velocity deficit in the center of the tunnel, which is presumably offset by velocities larger than U_∞ at the edges of the tunnel, where we did not

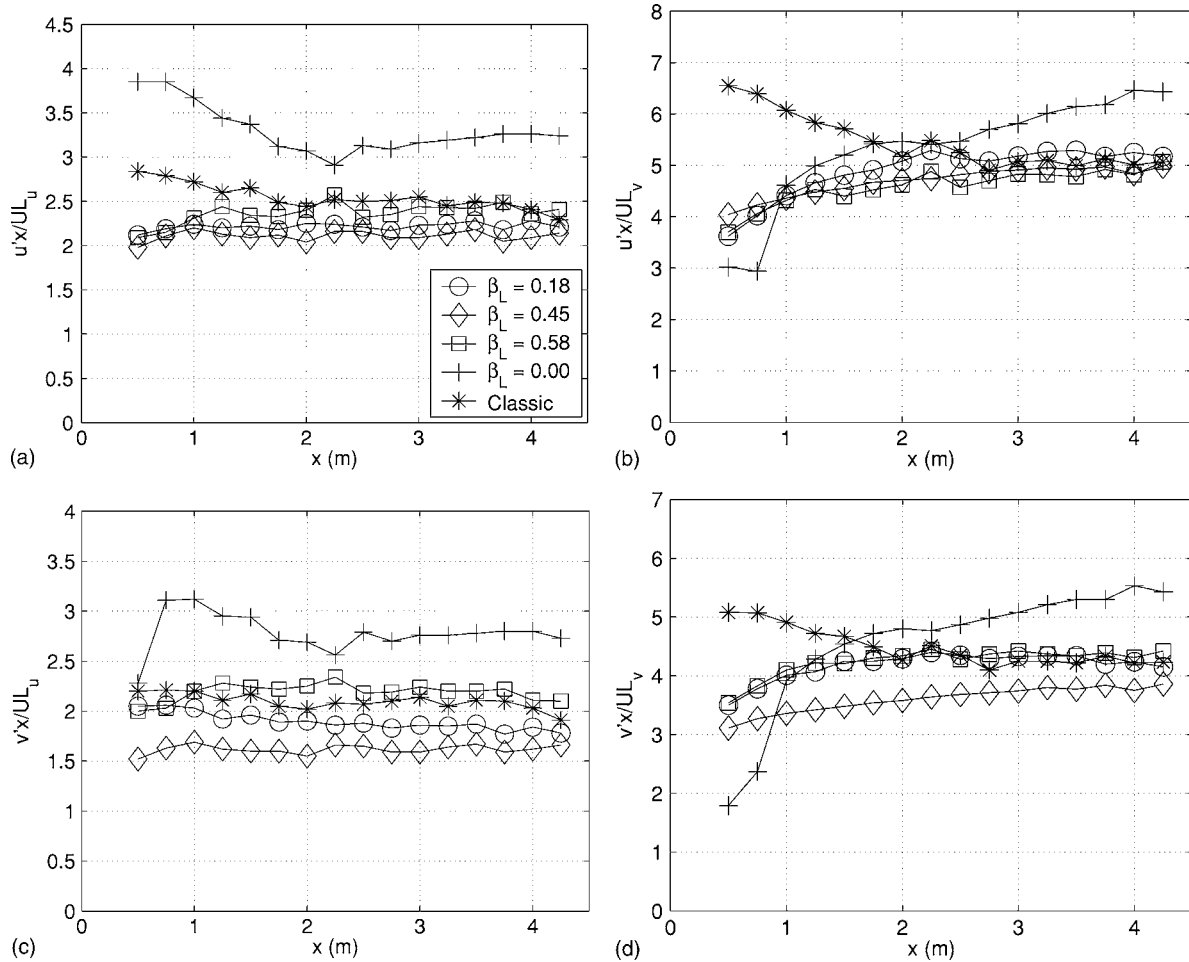


FIG. 11. Permanence of large eddies, $T=0.91$ m tunnel, $U_\infty=12$ m/s. See Fig. 3 for grid correspondence with β_L .

take measurements. In fact, this high- M_{eff} cross grid generates a wake-like turbulence around the centerline judging from the mean velocity deficit and the high turbulence intensities. In Sec. IV C, we report that the turbulence decay seems to scale with M_{eff} . Hence the distance $x=4.25$ m from the grids where traverses are taken may be considered to be effectively twice as far from the $M_{\text{eff}} \approx 57$ mm cross grids than from the $M_{\text{eff}} = 114$ mm cross grid. It may be concluded, subject to future confirmation with more such grids and more comprehensive measurements, that fractal cross grids produce as good transverse U homogeneity as classical grids but only much further away in multiples of M_{eff} (the mesh size

of our classical grid is $M=152$ mm and therefore factors larger than the mesh size of our fractal cross grids).

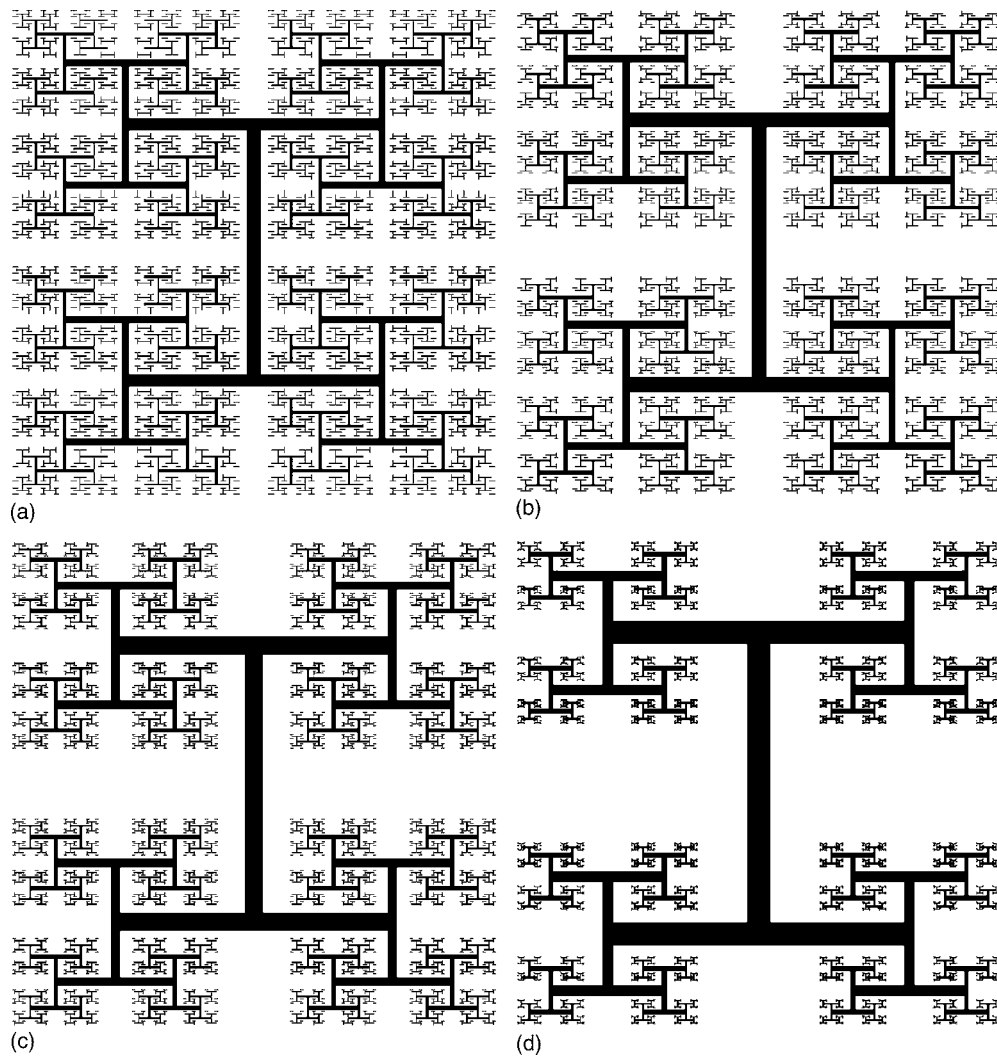
The homogeneity of u'/U and v'/U is very good for the fractal cross grids with $M_{\text{eff}} \approx 57$ mm and for the classical grid, but not so good, though perhaps broadly satisfactory around the centerline, for the fractal cross grid with M_{eff}

TABLE I. $T=0.91$ m tunnel I grid geometry. The errors on σ are estimated by assuming the thickness of each iteration to be accurate within plus/minus the diameter of the manufacturing cutting laser (0.15 mm).

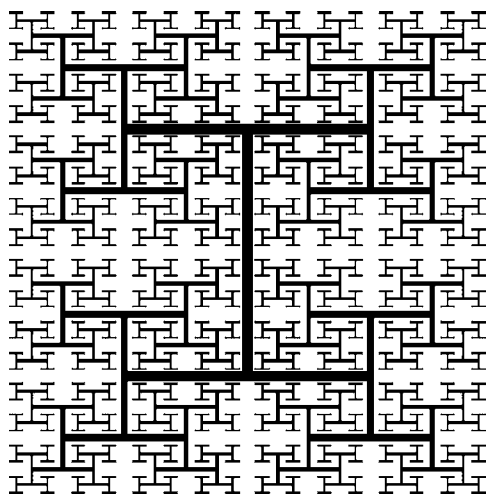
N	D_f	β_t	β_L	σ (%)	M_{eff} (mm)	t_r	R_t
6	1.68	-0.49	-0.38	25±1.0	50	43.8	0.47
6	1.79	-0.25	-0.21	25±1.7	31	34.0	0.49
6	1.87	-0.13	-0.11	25±2.1	25	29.2	0.51
6	1.98	0.00	0.00	25±2.5	21	24.9	0.53
5	2.00	0.40	0.69	31±1.4	36	5.0	0.67

TABLE II. $T=0.91$ m tunnel I grid geometry.

Grid	D_f 1.68	D_f 1.79	D_f 1.87	D_f 1.98	D_f 2.00
L_0 (mm)	570.3	524.8	503.1	483.9	468.3
L_1 (mm)	215.2	225.1	228.4	230.5	235.1
L_2 (mm)	81.2	96.6	103.7	109.8	118.0
L_3 (mm)	30.7	41.4	47.1	52.3	59.2
L_4 (mm)	11.6	17.8	21.4	24.9	29.7
L_5 (mm)	4.4	7.6	9.7	11.9	-
t_0 (mm)	43.8	34.0	29.2	24.9	20.0
t_1 (mm)	20.6	16.8	14.9	13.1	13.4
t_2 (mm)	9.7	8.3	7.6	6.9	8.9
t_3 (mm)	4.5	4.1	3.8	3.6	6.0
t_4 (mm)	2.1	2.0	2.0	1.9	4.0
t_5 (mm)	1.0	1.0	1.0	1.0	-

FIG. 12. Scaled diagrams of I grids: $N=6$ and $D_f=1.98, 1.87, 1.79,$ and 1.68 .

= 114 mm. A similar comment can be made again that fractal cross grids produce turbulence intensity profiles that are homogeneous but farther away in multiples of M_{eff} than classical grids. (By the way, it may be interesting to note that the

FIG. 13. Scaled diagram, I grid: $N=5$ and $D_f=2.0$.

peaks in the y profiles of v'/U and u'/U downstream of the $M_{\text{eff}}=114$ mm grid are positioned at distances from the center $y=0$, which are between M_{eff} and $2M_{\text{eff}}$.)

The large-scale isotropy indicator u'/v' takes values comparable to those obtained with active grids¹² (though larger than those obtained with classical grids^{9,10}) and is approximately homogeneous across y except for the cross grids with the two highest values of σ , which exhibit sudden growths in anisotropies far out from the centerline.

C. Turbulence decay

In Fig. 7, we plot the decay along the centerline of the Reynolds number $\text{Re}_\lambda \equiv u'\lambda/\nu$, where ν is the kinematic viscosity of the air at room temperature and λ is the Taylor microscale defined by $\lambda^2 \equiv u'^2 / \langle (\frac{1}{U} \frac{\partial u}{\partial t})^2 \rangle$, where u is the instantaneous fluctuating velocity in the x direction, and the angular brackets signify an average over time. [In the definition of λ , we have made use of the Taylor hypothesis $x = Ut$, which is known to be conservatively valid when u'/U , v'/U , and w'/U are less than about 10%, as is the case for all measurements in this paper. We calculate u'^2 and $\langle (\frac{1}{U} \frac{\partial u}{\partial t})^2 \rangle$ by appropriately integrating energy spectra such as those of

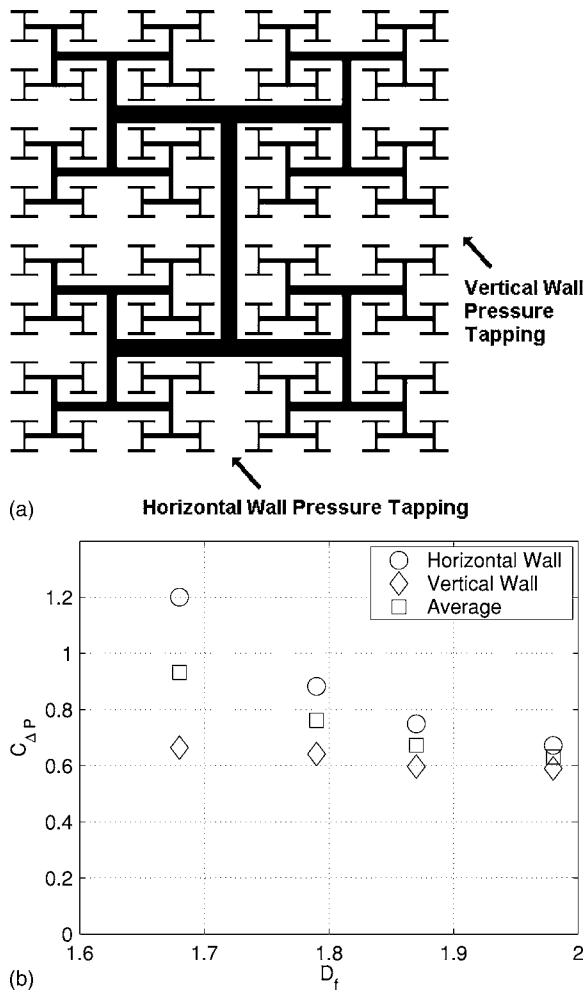


FIG. 14. Pressure tappings and $C_{\Delta P}$ values for different D_f . $T=0.91$ m tunnel.

Fig. 47 and resulting dissipation spectra. In all the cases presented in this paper, dissipation spectra were sufficiently well resolved for a sufficiently accurate estimation of $\langle (\frac{1}{U} \frac{\partial u}{\partial t})^2 \rangle$. The fractal cross grids with σ below 30% generate Reynolds numbers lower than the classical grid with $\sigma=44\%$. However, the fractal cross grid with $\sigma=40\%$ returns Reynolds numbers two to three times greater than the classical grid, but the turbulence it generates is far less homogeneous.

In Fig. 8, we plot the decay of turbulent intensities u' and v' on the centerline as the turbulence is convected downstream of the grid in the wind tunnel. It is interesting that u'/U and v'/U take very similar values for the three different cross grids with $\sigma \leq 29\%$ even though the normalized pressure drops $C_{\Delta P}$ are so different across each one of these grids. It is natural, however, to expect that $(u'/U)^2$ and $(v'/U)^2$ should be proportional to $C_{\Delta P}$, as is the case with wind tunnel turbulence generated by classical grids.^{9,14} The best way we have found to collapse these turbulence decay data without violating this proportionality involves the ratio of maximum to minimum thicknesses, t_r , and the effective mesh size. As shown in Fig. 8, this collapse is the following (it might be improved a bit if slightly different power relations between turbulence intensity and $C_{\Delta P}$ are allowed for the smaller values of t_r , specifically $t_r=2$ and 1, which cor-

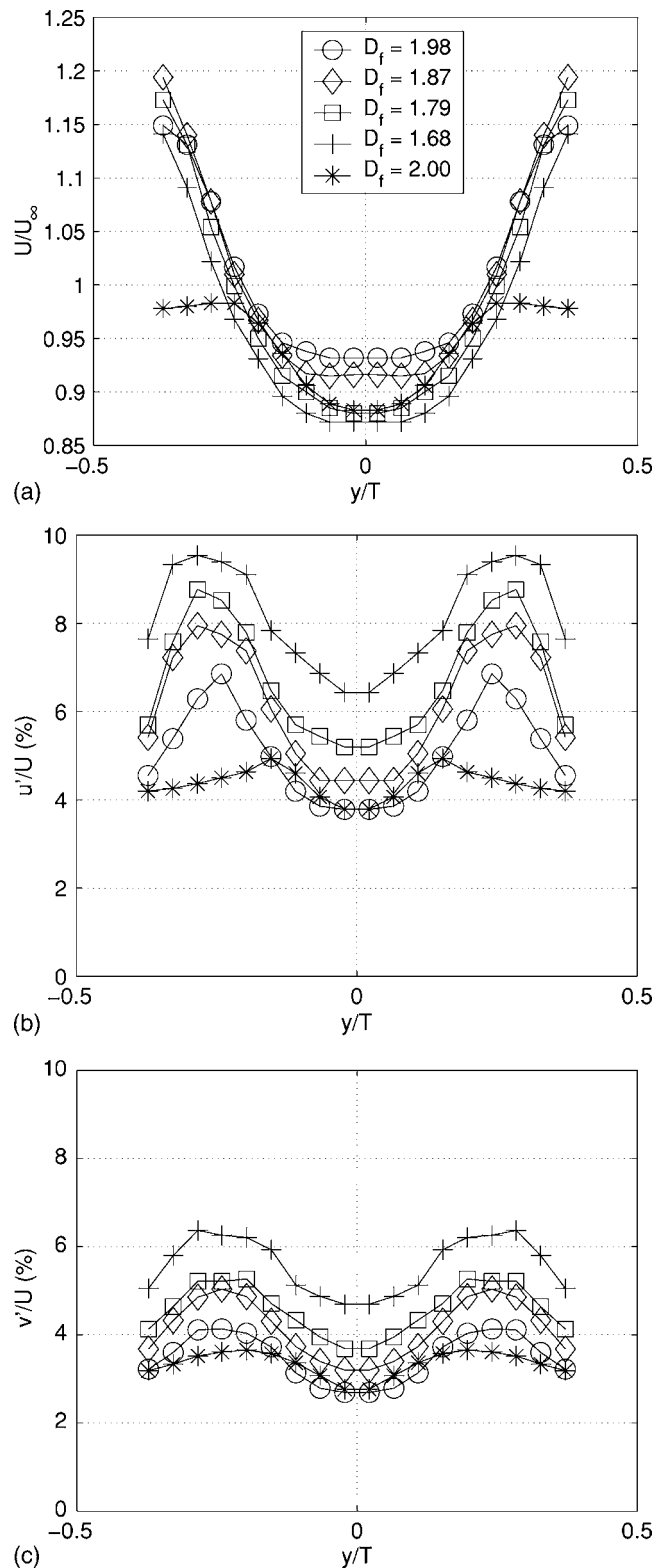


FIG. 15. I grids, $T=0.91$ m tunnel, $U_\infty=12$ m/s, $x=4.25$ m. Mean profiles in the y direction.

responds to the classical grid, but this fine point requires more data to be fully settled and is left for future study):

$$(u'/U)^2 = t_r^2 C_{\Delta P} f_u(x/M_{\text{eff}}), \tag{3}$$

$$(v'/U)^2 = t_r^2 C_{\Delta P} f_v(x/M_{\text{eff}}). \tag{4}$$

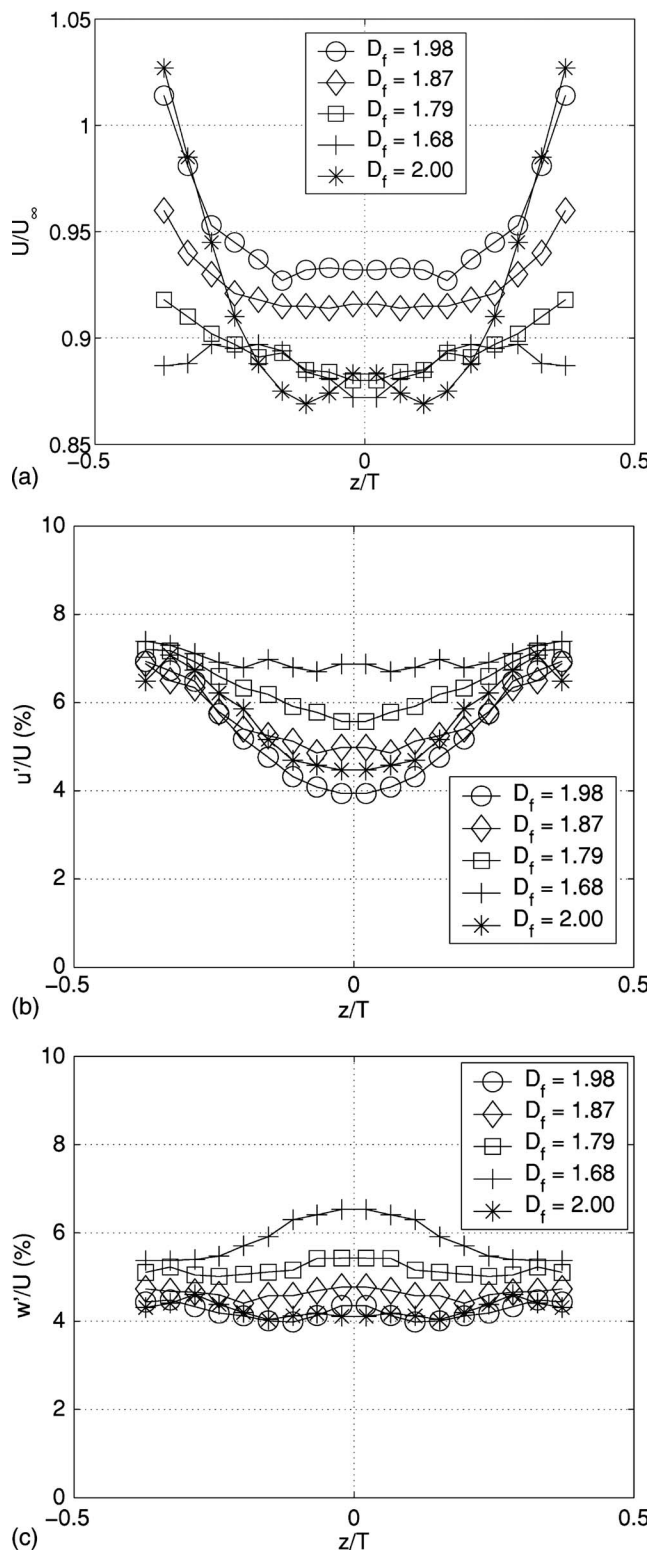


FIG. 16. I grids, $T=0.91$ m tunnel, $U_\infty=12$ m/s, $x=4.25$ m. Mean profiles in the z direction.

D. Power-law turbulence decay?

Assuming large- and small-scale isotropy, negligible turbulence production, and Taylor’s hypothesis, $-\frac{3}{2}U(du'^2/dx) = 15\nu u'^2/\lambda^2$, as originally shown by Taylor.¹⁵ Hence, a

TABLE III. $T=0.46$ m tunnel I grid geometry. The errors on σ are estimated by assuming the thickness of each iteration to be accurate within plus/minus the diameter of the manufacturing cutting laser (0.15 mm).

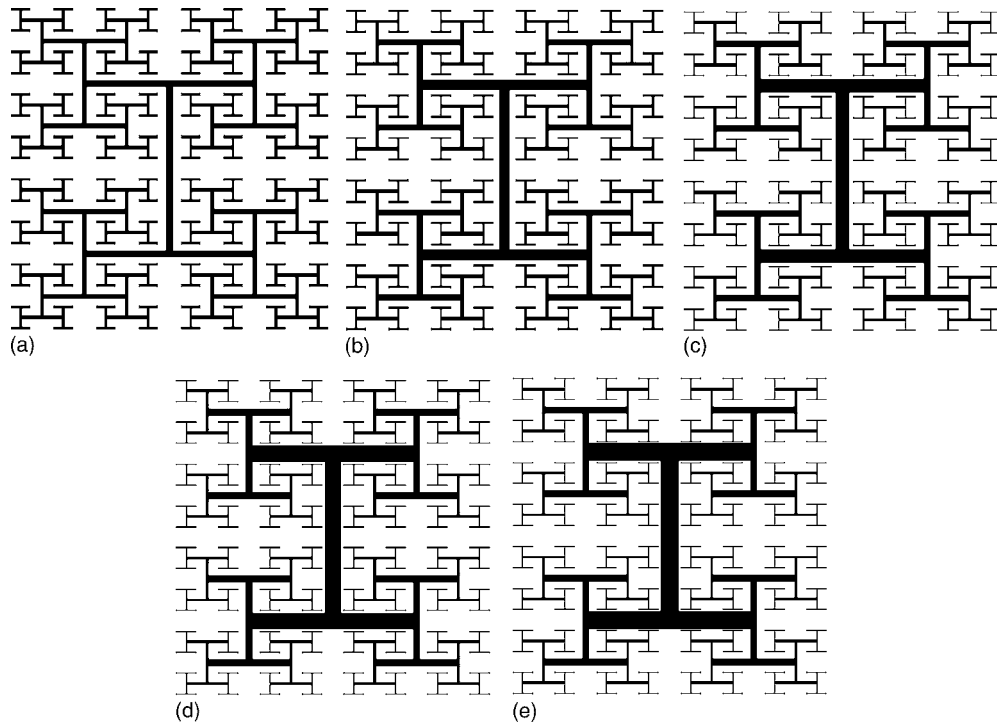
N	D_f	β_t	β_L	σ (%)	$M_{\text{eff}}(\text{mm})$	t_r	R_t
4	2.00	1.25	0.55	25 ± 1.4	36.9	2.5	0.74
4	2.00	0.30	0.23	25 ± 1.4	36.4	5.0	0.58
4	2.00	-0.04	-0.04	25 ± 1.4	35.9	8.5	0.49
4	2.00	-0.17	-0.21	25 ± 1.5	35.7	13.0	0.43
4	2.00	-0.25	-0.34	25 ± 1.5	35.5	17.0	0.39

power-law turbulence decay $u'^2 \sim (x-x_0)^{-n}$ (where x_0 is virtual origin) is only possible if $\lambda^2 \sim \nu(x-x_0)/U$.

The exponent n , which can be extracted from a best data fit, depends notoriously¹⁶ on the choice of the virtual origin x_0 . Writing $\lambda \sim (x-x_0)^s$, best data fits lead to different powers s for different values of x_0 . This is illustrated in Fig. 9, where we also show how n differs for different values of x_0 . We therefore try many different values of x_0 and choose the value that produces a well-defined $s=1/2$. Having chosen x_0 , we then find n , which fits $u'^2 \sim (x-x_0)^{-n}$ best. Figure 10 shows the results of our procedure. Choosing x_0 close to 0 gives exponents n similar to those obtained in previous studies of wind tunnel turbulence generated by classical^{10,16} and active¹⁷ grids where x_0 was indeed arbitrarily chosen or found to be small (effectively close to 0 by the scale of Fig. 10) by methods different from our λ -based one. However, choosing the value of x_0 for which $s=1/2$ gives values of n between 1.7 and 2.0 for the fractal cross grids and close to 2.3 for the classical grid. This x_0 turns out to lie between -0.5 and -1.2 m and is therefore well behind the grid.

The disagreement between previously published values of x_0 for classical grids and the value that we obtain from our λ -based method could have its cause in the small value of T/M of our classical grid and/or the relatively small streamwise extent of our measurements in multiples of M (up to about 28 M) away from the grid. To confirm this, we carried out hot wire measurements of turbulent streamwise velocities in the $T=0.46$ m wind tunnel with another classical biplanar grid made of square bars for which $T/M=14.4$ and $b=6$ mm. All these measurements were taken on the centerline from $x \approx 24 M$ to $x \approx 107 M$. We find $x_0 \approx 10 M$ by our λ -based method, and $\lambda^2 \sim (x-x_0)$ as well as an exponent $n \approx 1.39$ between $x \approx 24 M$ and $x \approx 107 M$, in good agreement with previous measurements.¹⁴

Power-law turbulence decay is often seen as resulting from the principle of permanence of large eddies.^{10,18} A particular consequence of power-law turbulence decay according to this principle is that $u'(x-x_0)/L_u$ (where L_u is the longitudinal integral length scale calculated, throughout this paper, by integrating the autocorrelation function of the velocity component u) is independent of x . In Fig. 11, we plot as functions of x , $u'x/UL_u$, $v'x/UL_u$, $u'x/UL_v$, and $v'x/UL_v$, where L_v is the lateral integral length scale (calculated, throughout this paper, by integrating the autocorrelation function of the velocity component v). The constancy of all these four quantities seems valid, particularly for the low blockage cross grids and for the two quantities involving L_u

FIG. 17. Scaled diagrams of space-filling I grids: $t_r=2.5, 5.0, 8.5, 13.0,$ and 17.0 .

instead of L_v . This is perhaps surprising considering the relative proximity of our measurement stations to the grids in multiples of M_{eff} and the relatively low values of T/M_{eff} .

E. First conclusions: Fractal cross grids

Our conclusions on the fractal cross grids can be summarized as follows:

- (i) The normalized static pressure drop is larger across fractal cross grids than across classical grids at equal blockage ratio. However, there is some, though limited, turbulence production downstream fractal cross grids that does not occur downstream classical grids.
- (ii) Statistical homogeneity is good for low blockage cross grids, though not as good as for classical grids. Statistical large-scale isotropy is comparable to that produced by active grids.
- (iii) The ratio t_r of outer to inner bar thicknesses and the effective mesh size are very important scaling parameters as they control the turbulence intensity (and therefore the Reynolds number too) independently from $C_{\Delta P}$, $(u'/U)^2 = t_r^2 C_{\Delta P} f_u(x/M_{\text{eff}})$, and $(v'/U)^2 = t_r^2 C_{\Delta P} f_v(x/M_{\text{eff}})$; see Eqs. (3) and (4).
- (iv) The turbulence decay observed is not in disagreement with power-law fits and the principle of permanence of large eddies. However, more extensive checks of large-scale and small-scale isotropy as well as homogeneity will be required to fully conclude on the nature of the turbulence decay behind fractal cross grids, in particular in order to assess the viability of our

λ -based method for estimating x_0 in the cross grid-generated flows.

V. TURBULENCE GENERATED BY FRACTAL I GRIDS

We constructed for the 0.91^2 m^2 tunnel four different planar I grids all with the same $t_{\text{min}}=1 \text{ mm}$, $\sigma=25\%$, and $N=6$ iterations. This fixes four of the five parameters required to completely determine a fractal I grid (see Sec. III A). The remaining parameter that we determine is the fractal dimension D_f , and we chose four values: $D_f=1.68, 1.79, 1.87,$ and 1.98 giving four different grids. These four grids have similar L_{max} because L_{max} turns out to be mostly constrained by the tunnel width. The purpose of these four grids is to determine the role of their fractal dimension at constant blockage ratio, minimum thickness, number of iterations, and tunnel size T .

TABLE IV. $T=0.46 \text{ m}$ tunnel I grid geometry.

Grid	t_r 2.5	t_r 5.0	t_r 8.5	t_r 13.0	t_r 17.0
L_0 (mm)	236.2	236.9	237.2	237.5	237.6
L_1 (mm)	118.1	118.4	118.6	118.7	118.8
L_2 (mm)	59.1	59.2	59.3	59.4	59.4
L_3 (mm)	29.5	29.6	29.7	29.7	29.7
t_0 (mm)	9.5	14.4	18.9	23.1	25.8
t_1 (mm)	7.0	8.4	9.3	9.8	10.0
t_2 (mm)	5.1	4.9	4.6	4.2	3.9
t_3 (mm)	3.8	2.9	2.2	1.8	1.5

We also constructed one more I grid for the 0.91^2 m^2 tunnel: it has $N=5$ iterations, $t_{\min}=4 \text{ mm}$, $D_f=2.0$, and a higher blockage $\sigma=31\%$ (which is made possible by the smaller number of iterations). The purpose of this extra I grid is to test dependencies on blockage and/or nondimensional parameters such as N . A complete quantitative description of these I grids is given in Tables I and II. Scaled diagrams are given in Figs. 12 and 13. The orientation of all the I grids used here was along the vertical z direction (see Fig. 14).

A. Better homogeneity for higher D_f

Due to the difference between the vertical and the horizontal directions of the I grids, two measurements of the static pressure drop across each I grid were taken using a Betz manometer, one at the midpoint of a vertical wall and the other at the midpoint of a horizontal wall (see Fig. 14). These measurements were taken for various mean flow velocities U_∞ upstream of the grid. In Fig. 14, we plot the dimensionless normalized static pressure drops $C_{\Delta P}$ at both tappings and for the five different fractal I grids shown in Figs. 12 and 13. The different values of $C_{\Delta P}$ between the two tappings indicate inhomogeneity of the flow near the grid. Clearly this inhomogeneity is progressively reduced as D_f tends toward its maximal value 2.

Qualitatively, a characteristic average value of $C_{\Delta P}$ is reflected in the power settings required for the wind tunnel to run. In the testing carried out, similar power levels were required for all $N=6$ I grids, thus implying that the drag was similar for all these grids. This might suggest that the $C_{\Delta P}$ measurements on the vertical wall might be a better indicator of overall grid drag than the $C_{\Delta P}$ measured on the horizontal wall, which is strongly dependent on the grid (see Fig. 14).

We set $U_\infty=12 \text{ m/s}$, and the mean y profiles, which we obtained far downstream from the grids ($x=4.25 \text{ m}$ in the 0.91^2 m^2 wind tunnel), all concur with the trend that homogeneity improves for higher D_f (see U/U_∞ , u'/U , and v'/U y profiles in Fig. 15).

The homogeneity of U/U_∞ in the z direction is good for all D_f particularly around the center (see Fig. 16, and note that U/U_∞ varies between 0.87 and 1.03 across all grids and for all values of z sampled), and the homogeneity of the w'/U z profiles also improves as D_f increases. Only the homogeneity of the u'/U z profile worsens as D_f increases, but not by much compared with the overall improvement in homogeneity as D_f increases.

We therefore conclude that, overall, the homogeneity of mean profiles improves as D_f increases, but is never as good as it is in turbulence generated by cross and classical grids. One may suspect by direct inspection of Fig. 12 that the lower the values of D_f , the higher the influence on profiles about the tunnel's centerline of the wake turbulence generated by the largest vertical bar. This point merits further study, but we leave it for future investigations as we are mainly concerned, in this paper, with finding fractal grid designs that produce as homogeneous a turbulence as possible.

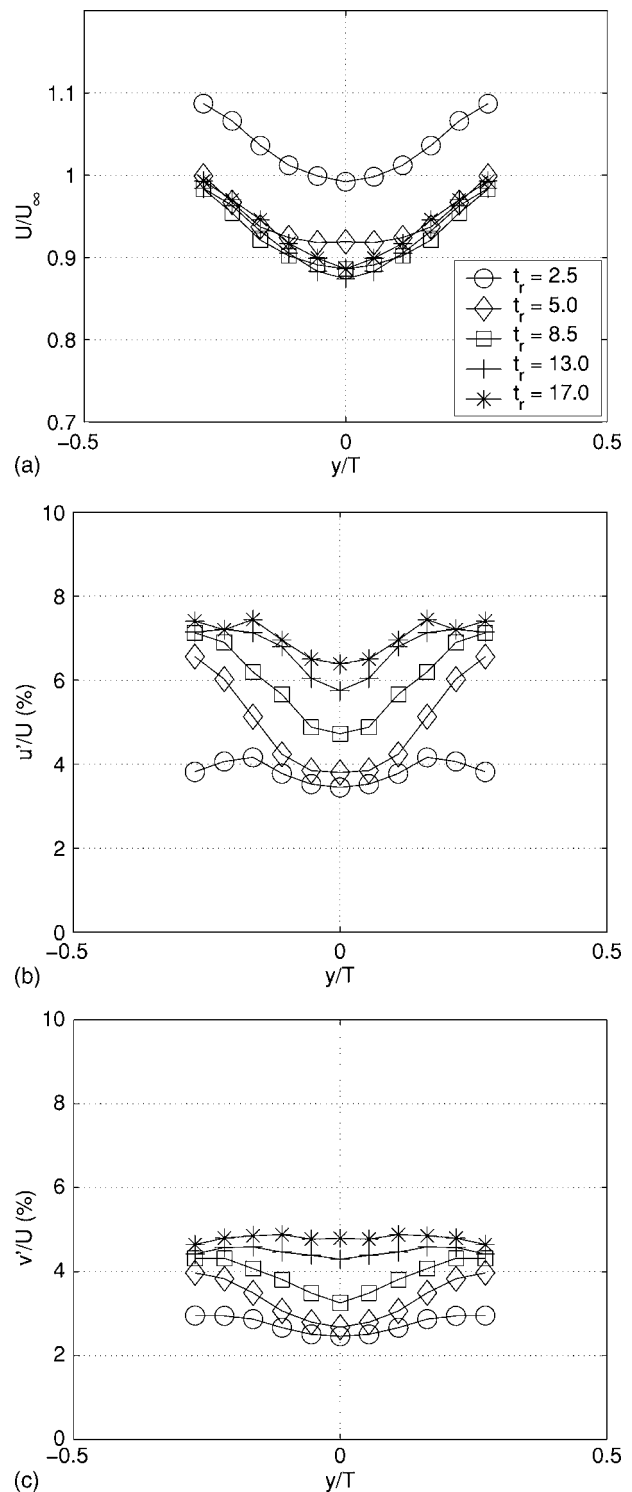


FIG. 18. Space-filling I grids, $T=0.46 \text{ m}$ tunnel, $U_\infty=10 \text{ m/s}$, $x=3.25 \text{ m}$. Mean profiles in the y direction.

B. Space-filling fractal I grids

To maximize our chances of achieving homogeneous turbulence, we designed and constructed five new fractal I grids all with $D_f=2$ (it is in this sense that these grids are “space-filling”). We kept $\sigma=25\%$ as with the previous $N=6$ I grids. We designed these five new grids for the $T=0.46 \text{ m}$ wind tunnel, which, even though smaller, has effectively a longer test section (it is approximately $7.8 T$ long). To iden-

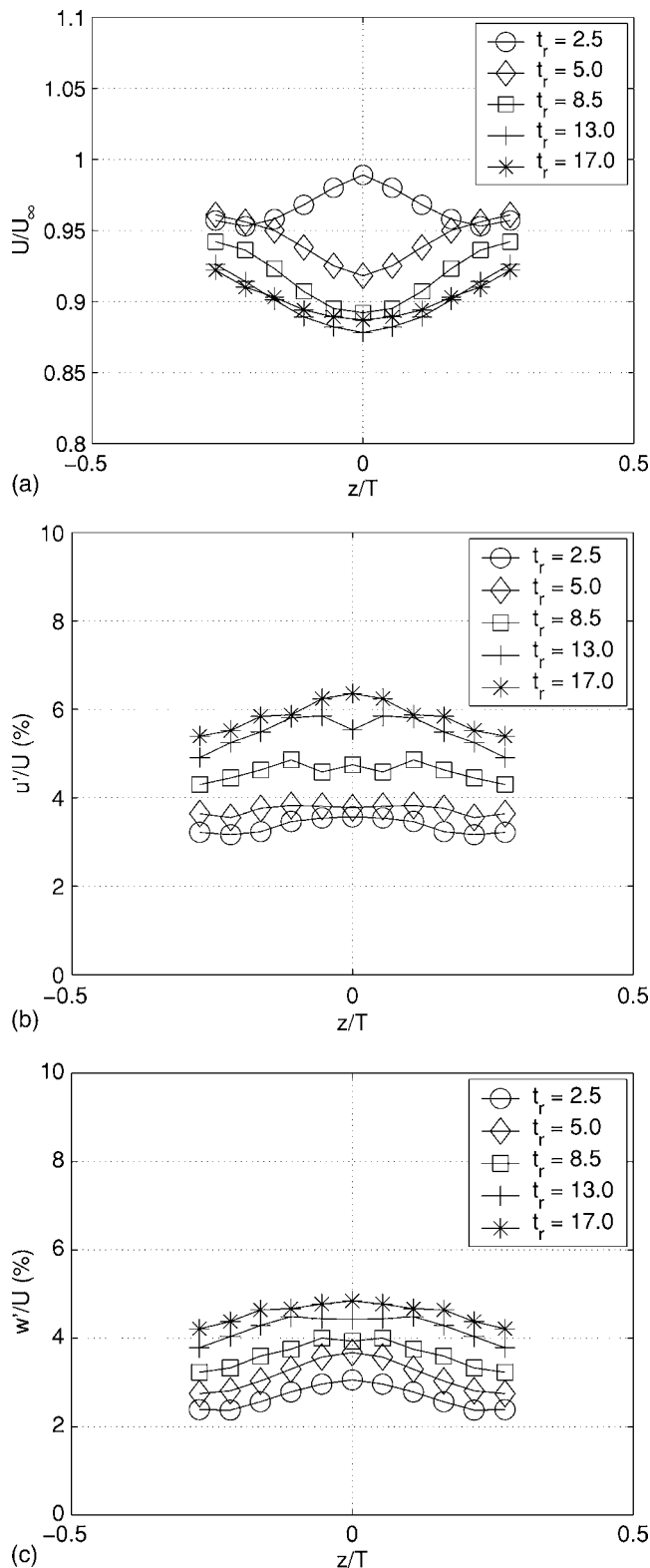


FIG. 19. Space-filling I grids, $T=0.46$ m tunnel, $U_\infty=10$ m/s, $x=3.25$ m. Mean profiles in the z direction.

tify which length scale or length scales control turbulence decay, it is useful to construct fractal I grids with the same values of M_{eff} , σ , L_{max} , and L_{min} , for example, in which case we can establish the role of t_{max} by varying it from grid to grid. Other such experiments will be needed in the future

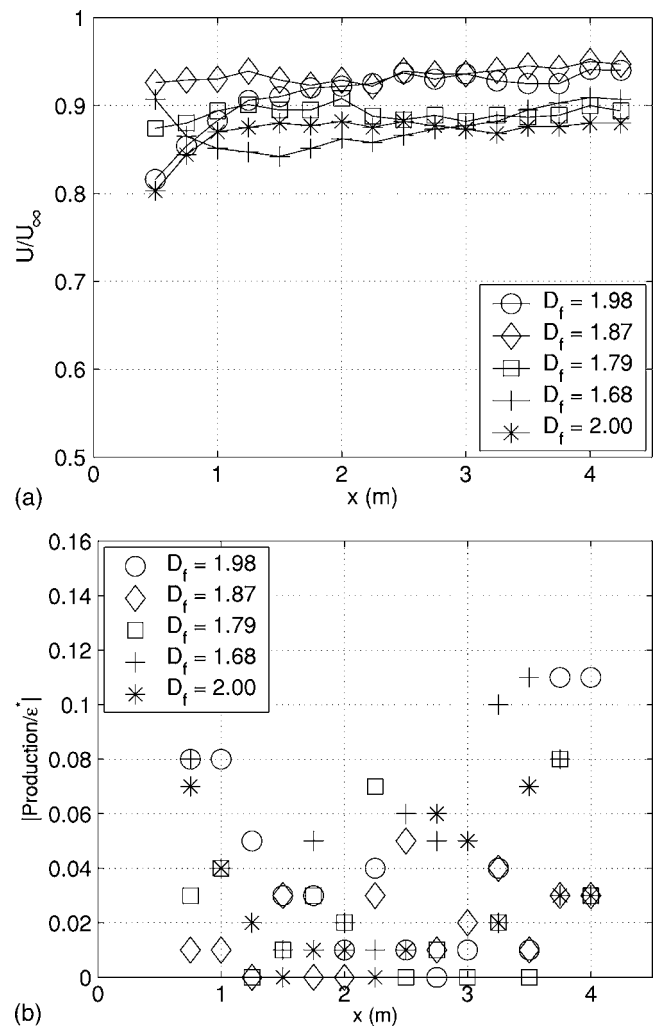


FIG. 20. Turbulence production, I grids $D_f \leq 2$, $T=0.91$ m tunnel, $U_\infty=10$ m/s.

where other length scales will be made to vary while most remain constant. Here we have set $N=4$ and $M_{\text{eff}}=36$ or 37 mm for all these new I grids. It is possible to widely vary t_r while only slightly varying M_{eff} within this narrow range because M_{eff} is predominantly controlled by R_L and N , which are both fixed to $1/2$ and 4, respectively. The five grids differ by $t_r=2.5, 5.0, 8.5, 13.0$, and 17.0. The lengths L_{max} and L_{min} also turn out to be about constant for these five grids. A complete quantitative description of these space-filling I grids is given in Tables III and IV. Scaled diagrams are given in Fig. 17.

C. Space-filling fractal I grids: Homogeneity

The normalized static pressure drop $C_{\Delta P}$ is approximately 0.75 at both pressure tappings (thus supporting the conclusion in Sec. V A that the static pressure drop's inhomogeneity is primarily controlled by D_f) and invariant with grid t_r . Setting $U_\infty=10$ m/s, U/U_∞ profiles at $x=3.25$ m are found to be quite homogeneous (see Figs. 18 and 19, and notice the values of U/U_∞ on the ordinate axes) and approximately independent of t_r (except for $t_r=2.5$). The homogeneity of the u'/U and v'/U y profiles improves ($t_r=2.5$ ex-

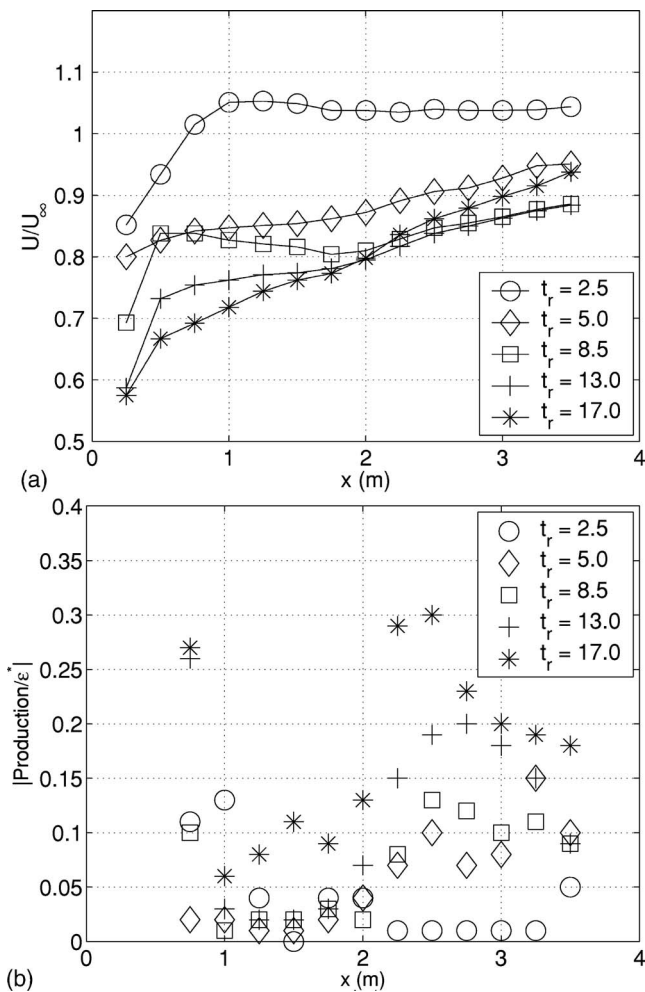


FIG. 21. Turbulence production, I grids $D_f=2$, $T=0.46$ m tunnel, $U_\infty=10$ m/s.

cepted) and that of the w'/U z profiles improves slightly as t_r increases (see Figs. 18 and 19). However, the homogeneity of the u'/U z profile worsens slightly as t_r increases, but by not much compared with the overall improvement in homogeneity as t_r increases (see Fig. 19).

We conclude that, overall, the homogeneity of mean profiles downstream of space-filling fractal I grids is satisfactory and, perhaps surprisingly, improves as t_r increases. We note that homogeneity regions at the centers of the mean profiles far downstream of our grids (including space-filling and non-space-filling ones) are invariably larger than five longitudinal and eight to ten lateral integral length scales.

D. Turbulence production by $\partial U/\partial x$

Fractal I grids do not generate significantly nonzero values of $\frac{\partial U}{\partial x}$ on the tunnel’s centerline when $D_f < 2$ (see Fig. 20). However, when $D_f=2$ production by nonzero values of $\frac{\partial U}{\partial x}$ increases with t_r up to values above about 10% of dissipation for t_r larger than about 10 (see Fig. 21; in this figure and Fig. 20 we used the same measure of dissipation as in Sec. IV B but with $\mathcal{P}=-u'^2 \frac{dU}{dx}$, the modulus of which is most probably an overestimate¹³).

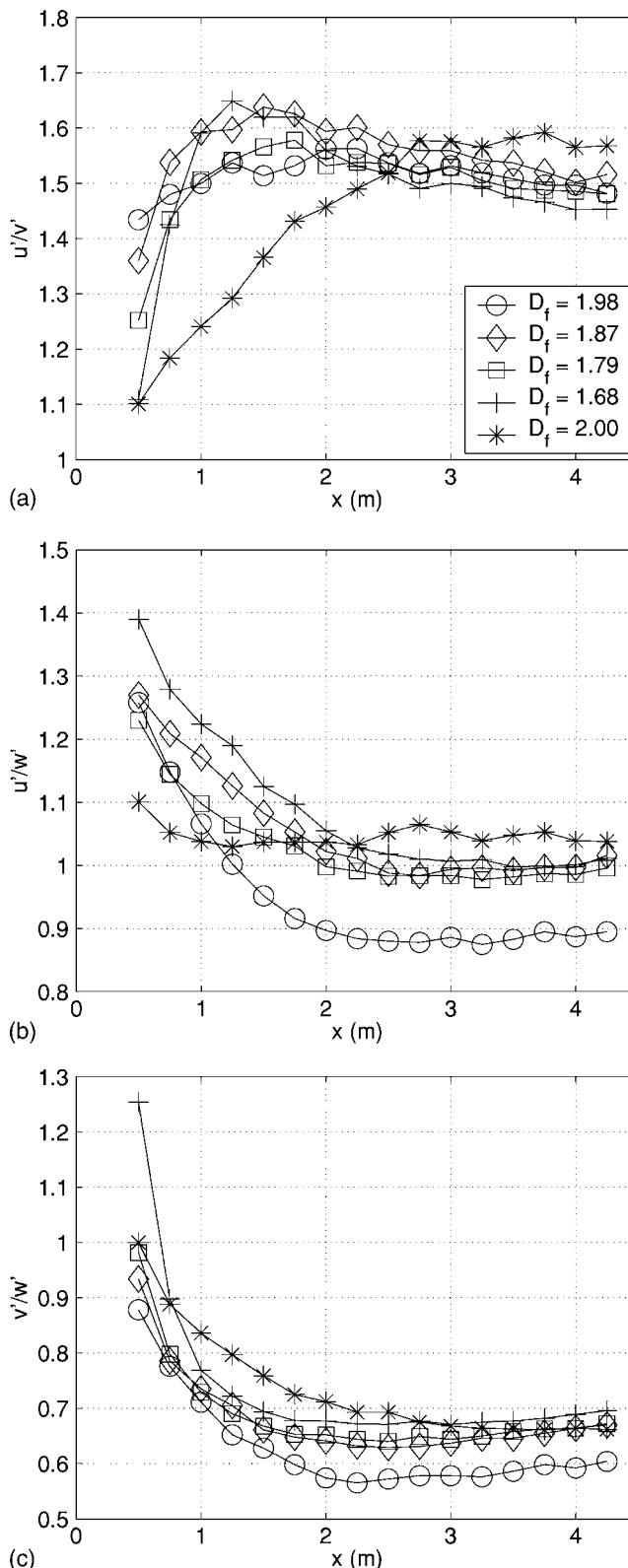


FIG. 22. Large-scale anisotropy, I grids $D_f \leq 2$, $T=0.91$ m tunnel, $U_\infty=12$ m/s.

E. Large-scale anisotropy

Figure 12 might suggest that fractal I grids with higher values of D_f generate turbulence with higher levels of large-scale anisotropy. However, as evidenced in Fig. 22, this is

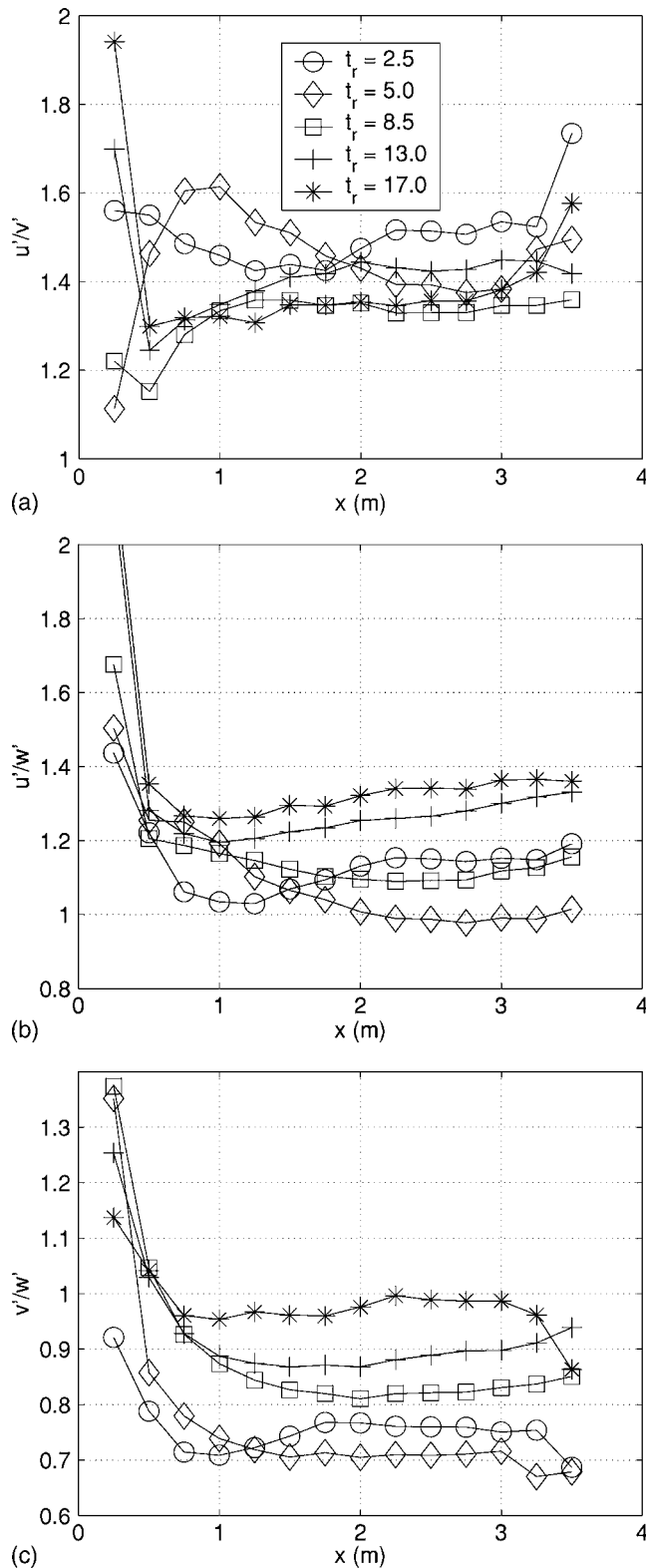


FIG. 23. Large-scale anisotropy, I grids $D_f=2$, $T=0.46$ m tunnel, $U_\infty=10$ m/s.

not the case. The values of u'/v' and v'/w' are sufficiently far from 1 to categorize the turbulence as anisotropic at the large scales. But there is no clear trend with D_f ; the anisotropy is by and large comparable for all fractal dimensions D_f .

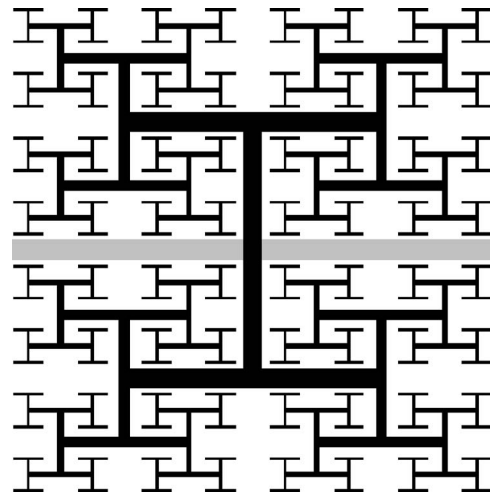


FIG. 24. Space-filling I grid with added central bar of thickness t_{max} .

The turbulence generated by the space-filling I grids (see Fig. 17) in the $T=0.46$ m wind tunnel is also significantly anisotropic, as shown in Fig. 23. In this case, however, a trend with t_r is observed: u'/w' and v'/w' increase as t_r increases ($t_r=2.5$ excepted).

These results seem to suggest that the large-scale turbulence anisotropy does not result solely or mostly from the largest scales of the I grids. All the scales of these grids are anisotropic and all of them seem to be contributing to the anisotropy of the turbulence. To test this hypothesis, we have added a bar of similar thickness to t_{max} (17 mm) to each space-filling I grid and measured the values of u'/v' , u'/w' , and v'/w' in the turbulence generated by these grids in the $T=0.46$ m wind tunnel at $x=3.25$ m. The addition of this bar increases the blockage from 25.0% to 28.7% (see Fig. 24). The results, plotted in Fig. 25, support the conclusion that the multiscale anisotropy of the fractal I grids is essential for the large-scale anisotropy of the resulting turbulence. Indeed, no clear trend can be extracted from Fig. 25; the addition of this large-scale bar can either increase or decrease the values of u'/v' , u'/w' , and v'/w' .

F. Turbulence decay

In Fig. 26, we plot the decay along the centerline of the Reynolds number Re_λ defined in Sec. IV C. U_∞ was set at 12 m/s in the $T=0.91$ m tunnel and at 10 m/s in $T=0.46$ m tunnel. There appears to be a trend whereby space-filling I grids with higher t_r generate higher Reynolds numbers ($t_r=2.5$ excepted). Considering the low blockage ratio of our fractal I grids ($\sigma=25\%$), these Reynolds numbers are rather high, particularly when compared with those of the turbulence generated by classical and cross grids with similar values of U_∞ and either similar or much higher values of σ (compare Fig. 26 with Fig. 7). However, the turbulence produced by the I grids is significantly less homogeneous and more anisotropic than the turbulence produced by classical and cross grids.

In Fig. 27, we plot the decay of turbulent intensity u'/U on the centerline as the turbulence is convected down the wind tunnel. It is natural to expect that $(u'/U)^2$ should be

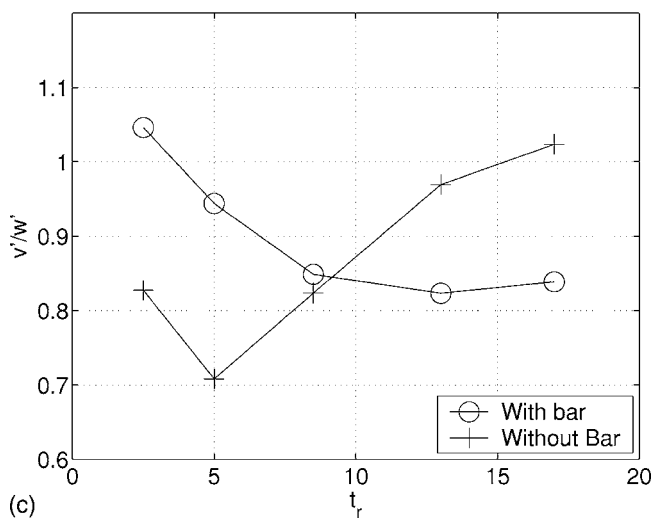
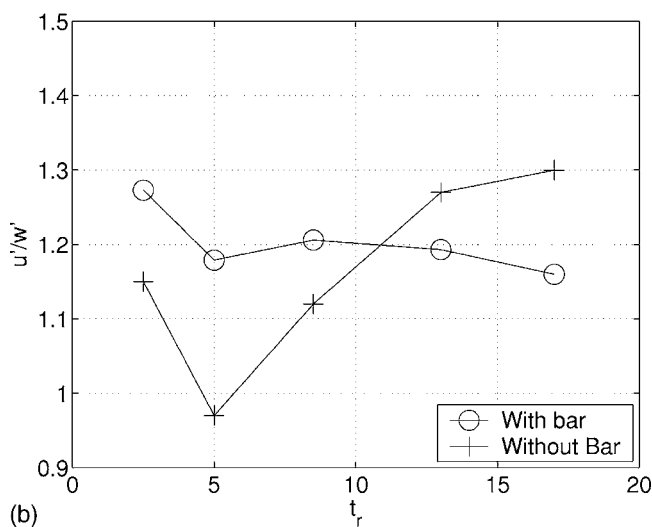
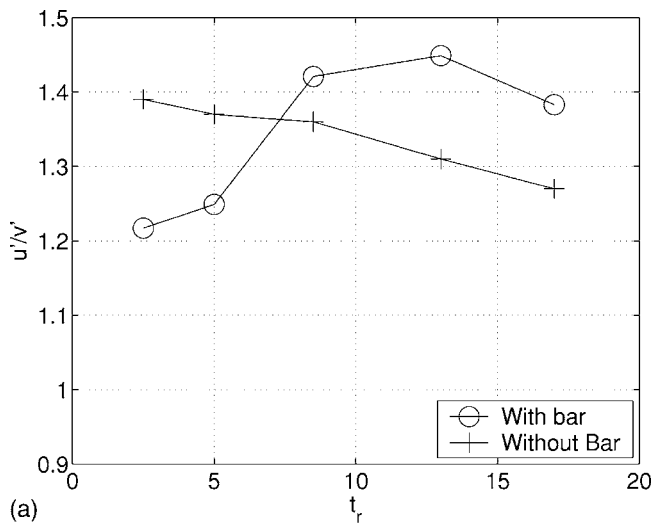


FIG. 25. Large-scale anisotropy, I grids with bar, $T=0.46$ m tunnel, $U_\infty = 10$ m/s.

proportional to $C_{\Delta P}$, as is the case with wind tunnel turbulence generated by classical grids.^{9,14} The best way we have found to collapse these turbulence decay data without violating this proportionality involves the ratio of maximum to

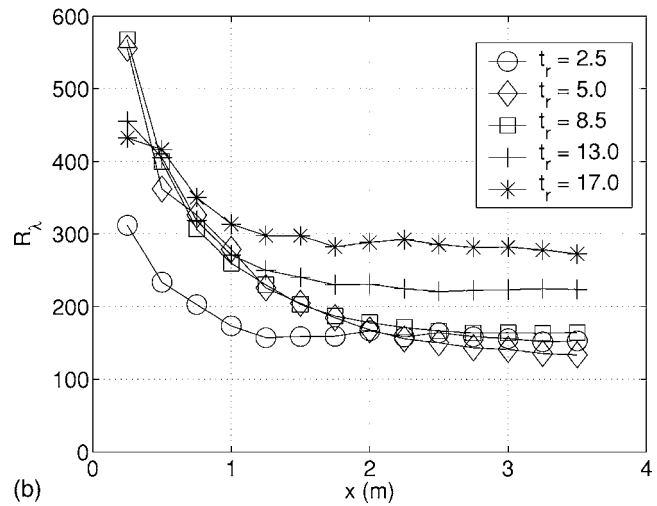
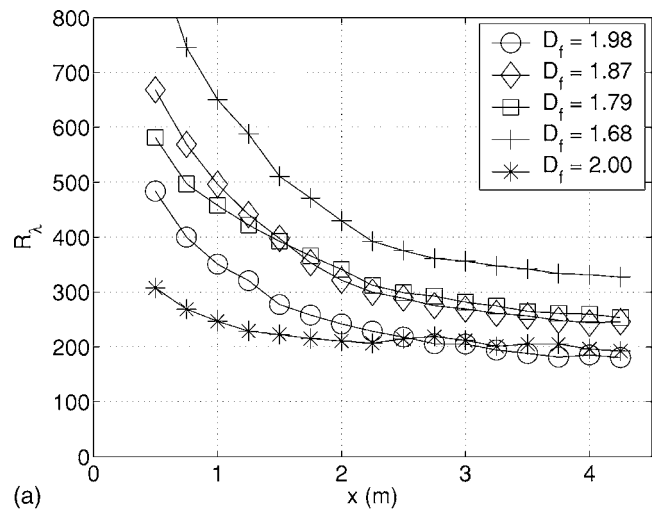


FIG. 26. Re_λ as a function of x measured in meters from the I grids. $U_\infty = 12$ m/s in the $T=0.91$ m tunnel and $=10$ m/s in the $T=0.46$ m tunnel.

minimum thicknesses, t_r , the effective mesh size M_{eff} , and the ratio T/L_{max} . As shown in Fig. 27, we find that

$$(u'/U)^2 = t_r C_{\Delta P} (T/L_{max})^2 fct(x/M_{eff}) \tag{5}$$

collapses the turbulence decay data generated by all fractal I grids in both wind tunnels. In this equation, $C_{\Delta P}$ is measured on the vertical wall in agreement with the observations concerning homogeneity and dependence on D_f made in Sec. V A in relation to Fig. 14 (see also the first sentence of Sec. V C). The data for v'/U and w'/U collapse in exactly the same way and with the same quality of collapse, and we also show v'/U in Fig. 27 but not w'/U for economy of space.

G. Power-law turbulence decay?

As explained in Sec. IV D and under the assumptions stated there, a power-law turbulence decay $u'^2 \sim (x-x_0)^{-n}$ is only possible if $\lambda^2 \sim [\nu(x-x_0)]/U$. Of these assumptions, the Taylor hypothesis can be applied to all I grid-generated flows as turbulence intensities are small enough in all our points of measurement. Turbulence production may be considered small, though not always negligible, for all I grids with $D_f \leq 2$ and t_r smaller than about 10. However, there is very

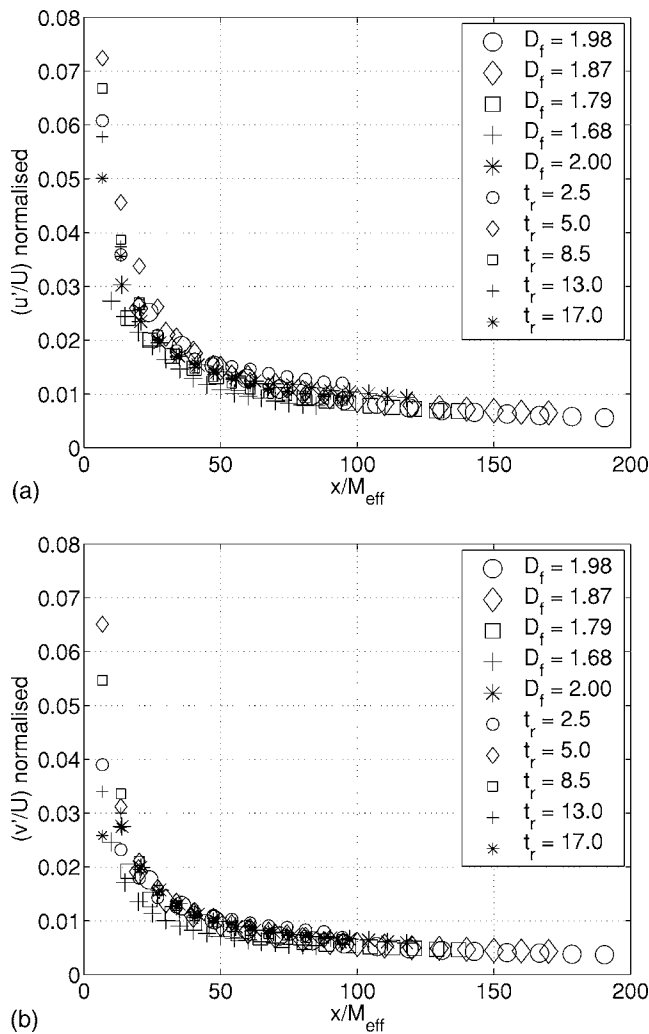


FIG. 27. Turbulence decay, I grids. u'/U and v'/U are normalized by $\sqrt{t_r C_{\Delta P}(T/L_{\text{max}})}$. $U_{\infty} = 12$ m/s in $T = 0.91$ m tunnel and $U_{\infty} = 10$ m/s in $T = 0.46$ m tunnel.

significant production in the flows generated by I grids with $D_f = 2$ and $t_r > 10$ and there is also significant large-scale anisotropy in the turbulence generated by all I grids. In spite of these shortcomings, we do attempt to find best data fits for $\lambda \sim (x - x_0)^s$ and therefore values of s as a function of the virtual origin x_0 . However, we calculate the Taylor microscale in two different ways: (i) by directly applying the definition $\lambda^2 \equiv u'^2 / \langle (\frac{1}{U} \frac{\partial u}{\partial t})^2 \rangle$ given in Sec. IV C and (ii) by using the definition ϵ^* of the kinetic energy dissipation rate per unit mass given in Sec. IV B but with $\mathcal{P} = -u'^2 \frac{dU}{dx}$, the modulus of which is most probably an overestimate.¹³ This definition of dissipation takes into account large-scale isotropy and, partly, production by $\frac{\partial U}{\partial x}$ (it ignores the correction due to incompressibility¹³) but is not very accurate in its determination of gradients along x . By equating ϵ^* to $15\nu \langle (\frac{1}{U} \frac{\partial u}{\partial t})^2 \rangle$ (where we make use of the Taylor hypothesis $x = Ut$ and assume turbulence isotropy), we obtain a second, indirect way of rather crudely estimating the Taylor microscale, $\lambda^* = (15\nu u'^2 / \epsilon^*)^{1/2}$. We measure both λ and λ^* and note that λ^* turns out to be typically larger than λ . That these two measurements yield slightly different values should not be sur-

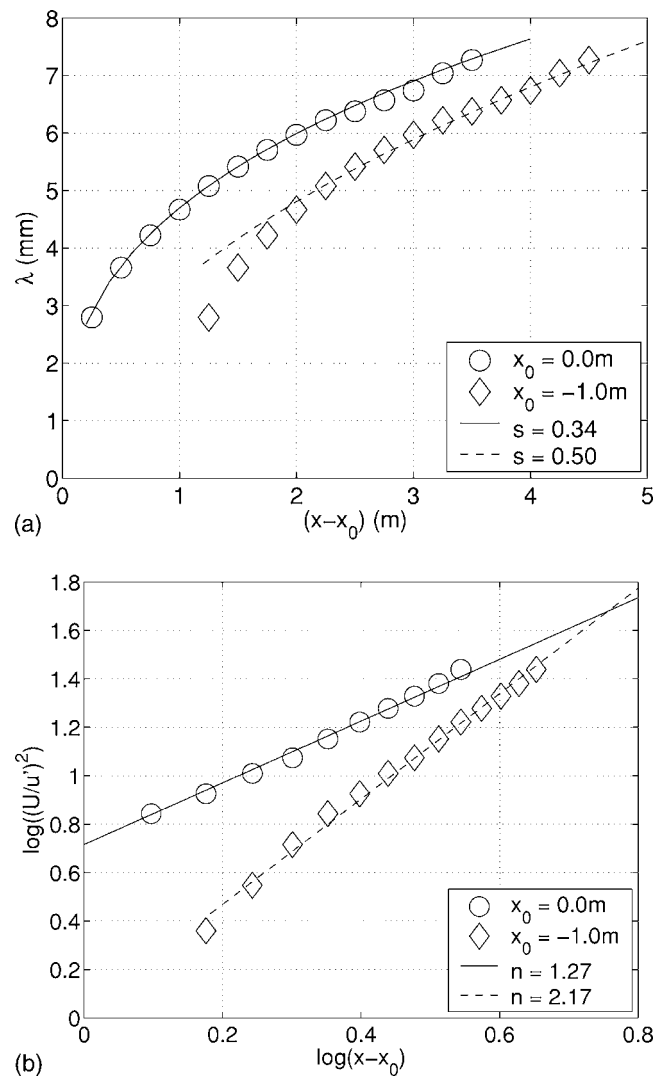


FIG. 28. Space-filling I grid, $t_r = 17$, $T = 0.46$ m tunnel, $U_{\infty} = 10$ m/s. Taylor microscale λ as a function of $x - x_0$ and $\log(U/u')^2$ as a function of $\log(x - x_0)$ for two values of x_0 . Best power-law fits are shown for both values of x_0 . x and x_0 are in meters.

prising as there are various inaccuracies in the determination of ϵ^* and uncertainties surrounding the assumptions leading to $\epsilon^* = 15\nu \langle (\frac{1}{U} \frac{\partial u}{\partial t})^2 \rangle$, the main ones being small-scale and large-scale anisotropy and good homogeneity. In the previous subsection, we provided evidence for significant large-scale anisotropy, which must therefore be an important contributor in the discrepancy between λ and λ^* .

If we are to choose the virtual origin x_0 , which satisfies $s = 1/2$, it is important to estimate the Taylor microscale in two different ways and therefore address the issue of how well we estimate it, particularly because of the uncertainties surrounding the assumptions leading to $s = 1/2$. For each x_0 , we determine the best-fit values of s and s^* in $\lambda \sim (x - x_0)^s$ and $\lambda^* \sim (x - x_0)^{s^*}$ and also the best-fit values of n in the assumed power-law $u'^2 \sim (x - x_0)^{-n}$. Examples of results are plotted in Figs. 28 and 29. If x_0 is chosen so as to set s^* rather than s equal to $1/2$, then our results are not inconsistent with power-law decay and $1 \leq n \leq 2$ for all I grids in

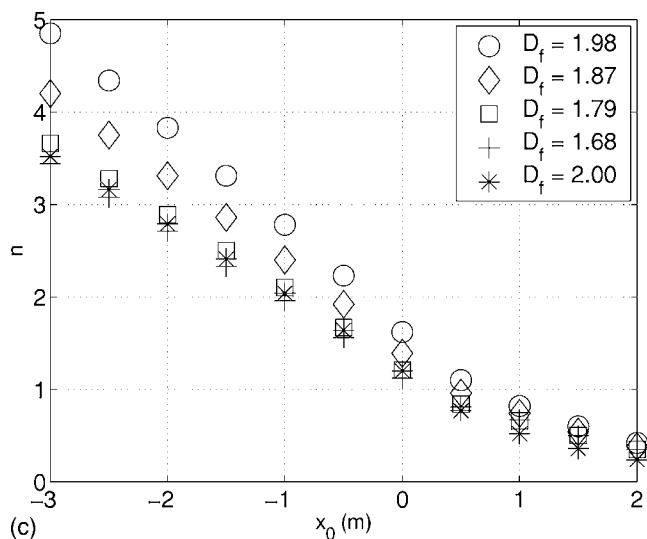
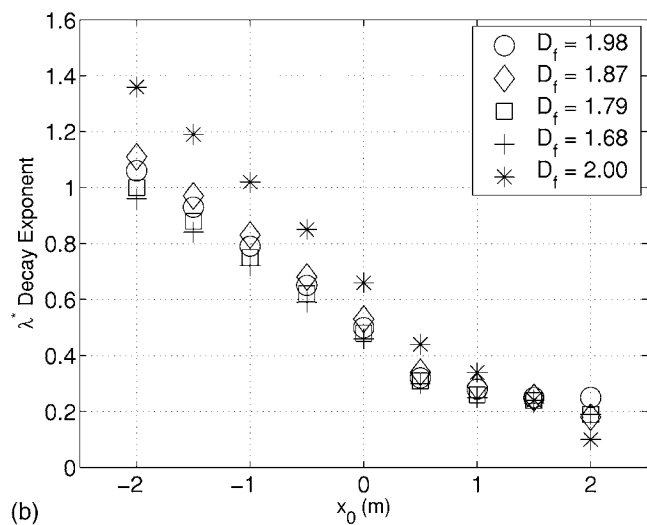
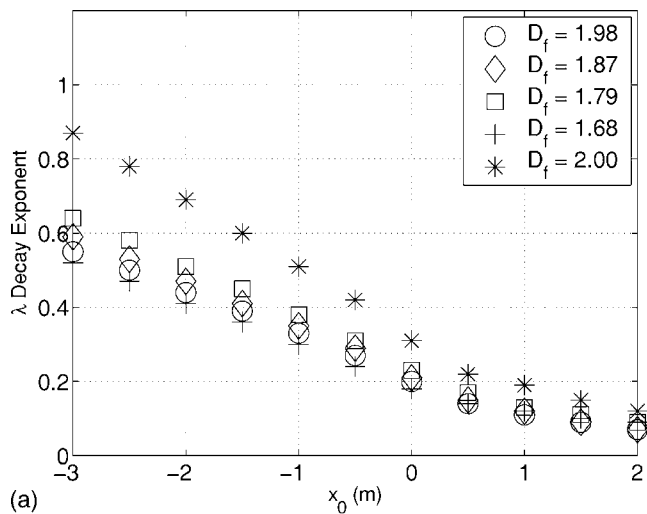


FIG. 29. I grids in $T=0.91$ m tunnel, $U_\infty=12$ m/s. Exponents s , s^* , and n as functions of x_0 (in meters).

both tunnels. It must be stressed that this conclusion does not mean that λ^* is a better estimate of the Taylor microscale than λ (which it probably is not) as it is not known whether the turbulence generated by I grids does indeed decay as a

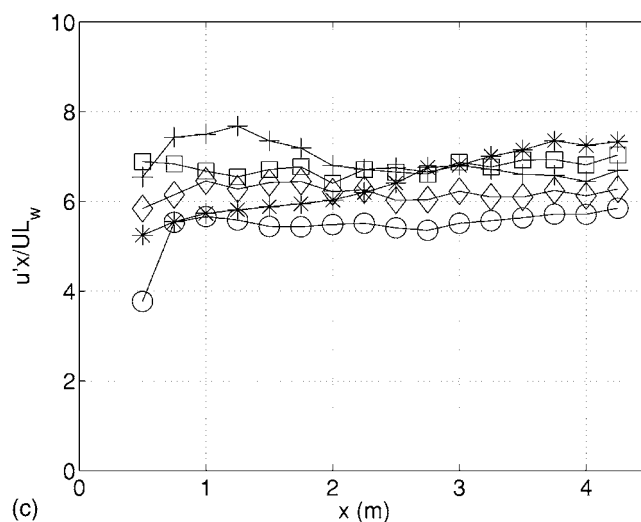
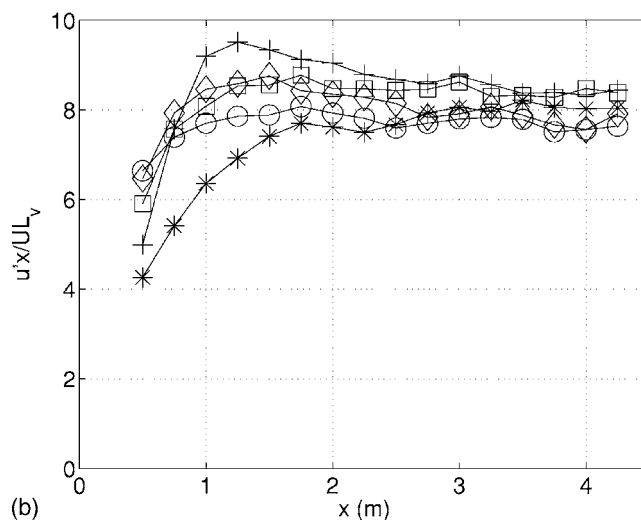
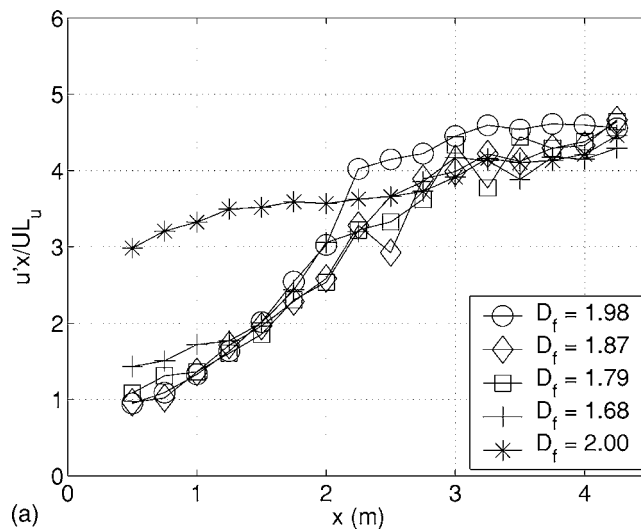


FIG. 30. Permanence of large eddies, I grids in $T=0.91$ m tunnel, $U_\infty=12$ m/s.

power law, and if so, with what power n . Our conclusion is a weak one and is stated in terms of two negatives: not inconsistent.

Finally, in Figs. 30 and 31 we make use of the longitudi-

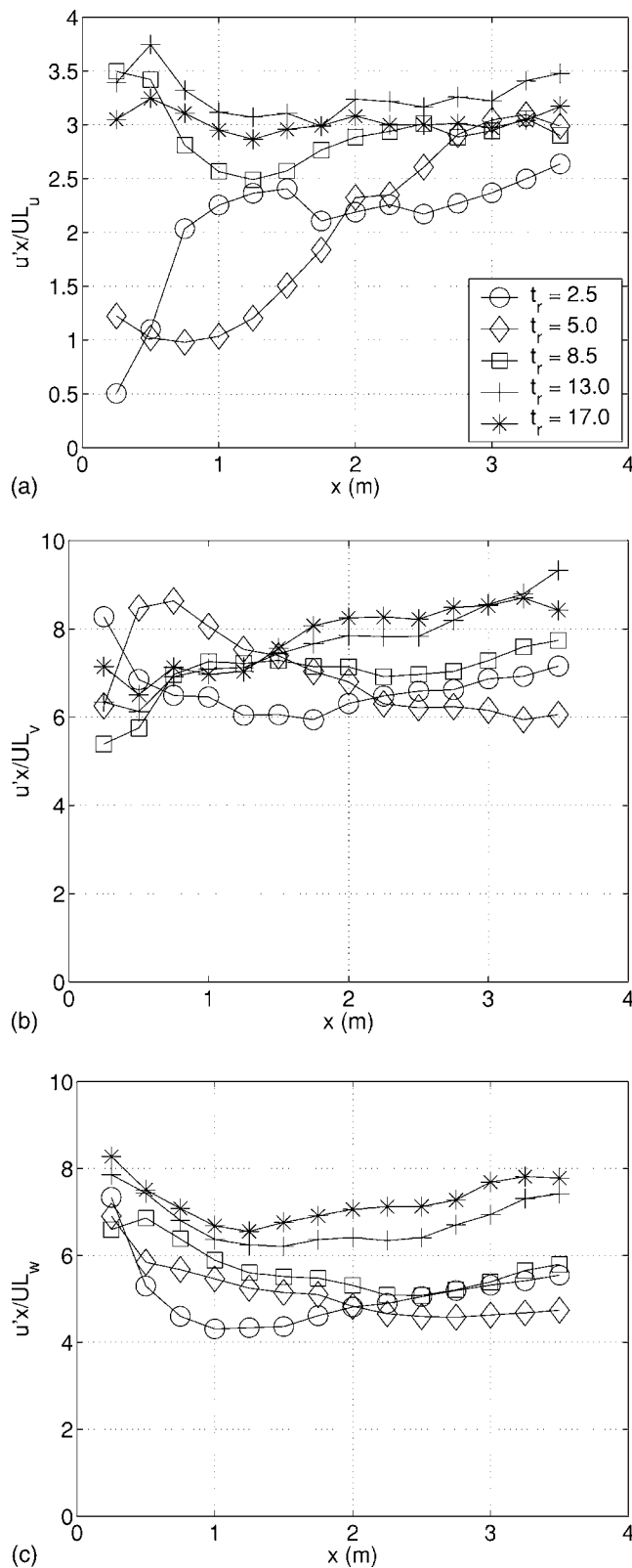


FIG. 31. Permanence of large eddies, space-filling I grids, $T=0.46$ m tunnel, $U_{\infty}=10$ m/s.

dinal integral length scale L_u and the two lateral integral length scales L_v and L_w (L_w is calculated by integrating the autocorrelation function of w) and plot as functions of x , $u'x/UL_u$, $u'x/UL_v$, and $u'x/UL_w$ for all I grids in both wind

TABLE V. $T=0.46$ m tunnel square grid geometry. The errors on σ are estimated by assuming the thickness of each iteration to be accurate within plus/minus the diameter of the manufacturing cutting laser (0.15 mm).

N	D_f	β_t	β_L	σ (%)	M_{eff} (mm)	t_r	R_t
4	2.00	1.32	0.58	25 ± 2.0	26.6	2.5	0.74
4	2.00	0.32	0.25	25 ± 2.0	26.5	5.0	0.58
4	2.00	-0.03	-0.03	25 ± 2.0	26.4	8.5	0.49
4	2.00	-0.16	-0.20	25 ± 2.0	26.3	13.0	0.43
4	2.00	-0.24	-0.33	25 ± 2.0	26.2	17.0	0.39

tunnels. By and large, these quantities seem constant for large enough values of x , thereby suggesting that the I grid turbulence data are not inconsistent with the principle of permanence of large eddies.

H. Second conclusions: Fractal I grids

Our conclusions on the fractal I grids can be summarized as follows:

- Statistical homogeneity improves with increasing D_f . For $D_f=2$, it is satisfactory and improves with increasing t_r . In this space-filling case, the normalized static pressure drop is invariant with t_r .
- Not much turbulence production occurs by $\frac{\partial U}{\partial x}$ when $D_f < 2$, but when $D_f=2$ such production increases with t_r up to values well above about 10% of dissipation for t_r larger than about 10.
- Large-scale turbulence anisotropy is generated by all anisotropic scales on the fractal I grids.
- The ratio t_r of outer to inner bar thicknesses, the effective mesh size, and the ratio T/L_{max} are the scaling parameters that control turbulence intensities u'/U , v'/U , and w'/U independently from $C_{\Delta P}$. For example, $(u'/U)^2 = t_r C_{\Delta P} (T/L_{\text{max}})^2 f(x/M_{\text{eff}})$; see Eq. (5).
- The turbulence decay observed is not in disagreement with power-law fits and the principle of permanence of large eddies. However, more extensive checks of large-scale and small-scale isotropy as well as homogeneity will be required to fully conclude on the nature of the turbulence decay behind fractal I grids, in particular in order to assess the viability of our

TABLE VI. $T=0.46$ m tunnel square grid geometry.

Grid	t_r 2.5	t_r 5.0	t_r 8.5	t_r 13.0	t_r 17.0
L_0 (mm)	236.9	237.2	237.5	237.7	237.8
L_1 (mm)	118.5	118.6	118.8	118.9	118.9
L_2 (mm)	59.2	59.3	59.4	59.4	59.5
L_3 (mm)	29.6	29.7	29.7	29.7	29.7
t_0 (mm)	7.0	10.7	14.2	17.2	19.2
t_1 (mm)	5.2	6.3	6.9	7.3	7.5
t_2 (mm)	3.8	3.7	3.4	3.1	2.9
t_3 (mm)	2.8	2.1	1.7	1.3	1.1

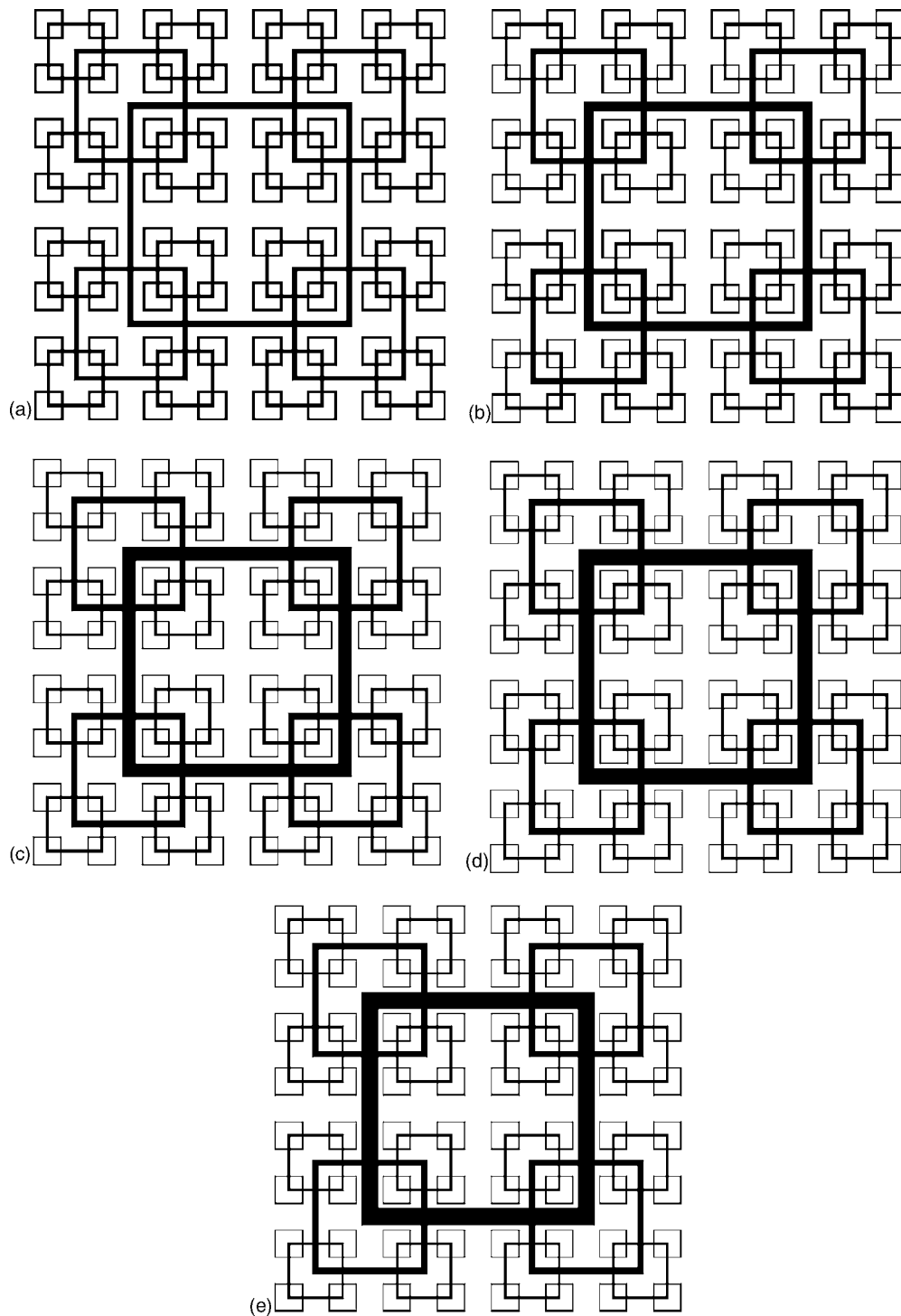


FIG. 32. Scaled diagrams of space-filling square grids for the $T=0.46$ m tunnel: $t_r=2.5, 5.0, 8.5, 13.0,$ and 17.0 .

λ -based method for estimating x_0 in these I grid-generated flows.

VI. TURBULENCE GENERATED BY SPACE-FILLING FRACTAL SQUARE GRIDS

We constructed for the $T=0.46$ m wind tunnel (test section's length $\approx 7.8 T$) five different planar fractal square grids all with $D_f=2$ (space-filling) for best homogeneity, the

same $\sigma=25\%$ (which is also the blockage ratio of nine out of the ten I grids), $N=4$ (as for the space-filling I grids), and $M_{\text{eff}} \approx 26.5$ mm for all grids. It is possible to widely vary t_r , while only slightly varying M_{eff} within a narrow range. The five space-filling square grids therefore differ by their values of t_r , and we choose the same five values of t_r as for the five space-filling I grids: $t_r=2.5, 5.0, 8.5, 13.0,$ and 17.0 . By square construction and tunnel width constraint, $L_{\text{max}}=237.4$ mm and $L_{\text{min}}=29.7$ mm for all five grids. A complete

TABLE VII. $T=0.91$ m tunnel square grid geometry. The errors on σ are estimated by assuming the thickness of each iteration to be accurate within plus/minus the diameter of the manufacturing cutting laser (0.15 mm).

N	D_f	β_t	β_L	σ (%)	M_{eff} (mm)	t_r	R_t
5	2.00	0.00	0.00	25 ± 2.0	26.6	17.0	0.49
5	2.00	-0.18	-0.21	25 ± 1.7	28.6	28.0	0.43

quantitative description of these space-filling fractal square grids is given in Tables V and VI. Scaled diagrams are given in Fig. 32.

The purpose of these five grids is to make a start toward identifying which length scale or length scales control turbulence decay. In this particular case, we keep M_{eff} , σ , L_{max} , and L_{min} constant, and vary only t_{max} and t_{min} . Other such experiments may be needed where other length scales are made to vary while most remain constant.

For the purpose of investigating the effects of the wind tunnel width T , we constructed two space-filling fractal square grids with similar specifications to the five previous square grids but larger so as to fit into the test section of the $T=0.91$ wind tunnel (test section's length $\approx 5.25 T$). For both of these larger square grids, $D_f=2.0$, $\sigma \approx 25\%$, $N=4$, and the value of M_{eff} is very close to that of the five smaller square grids. It is again possible to widely vary t_r , while only slightly varying M_{eff} within a narrow range. Hence, the two grids differ by their values of t_r : $t_r=17.0$ and 28.0 . L_{max} and L_{min} are about the same for both grids. A complete quantitative description of these space-filling fractal square grids is given in Tables VII and VIII. A fairly faithful pictorial description is given in Fig. 33.

A. Homogeneity and turbulence production by $\partial U/\partial x$

The normalized static pressure drop $C_{\Delta P}$ is found to lie between 0.6 and about 0.7 (the value for space-filling I grids is ≈ 0.75) at both pressure tappings and in both wind tunnels and for all our space-filling fractal square grids. $C_{\Delta P}$ is therefore, to first approximation, invariant with t_r (in fact, we observe a very small trend upwards with increasing t_r). (It may also be worth mentioning that the space-filling square grids have a $C_{\Delta P}$ that is about 15% lower than that of the space-filling I grids in the same wind tunnel even though the

TABLE VIII. $T=0.91$ m tunnel square grid geometry.

Grid	$\beta_L-0.18$	β_L 0.00
L_0 (mm)	483.3	471.2
L_1 (mm)	234.4	235.6
L_2 (mm)	113.7	117.8
L_3 (mm)	55.1	58.9
L_4 (mm)	26.7	29.5
t_0 (mm)	30.8	23.8
t_1 (mm)	13.4	11.7
t_2 (mm)	5.8	5.8
t_3 (mm)	2.5	2.8
t_4 (mm)	1.1	1.4

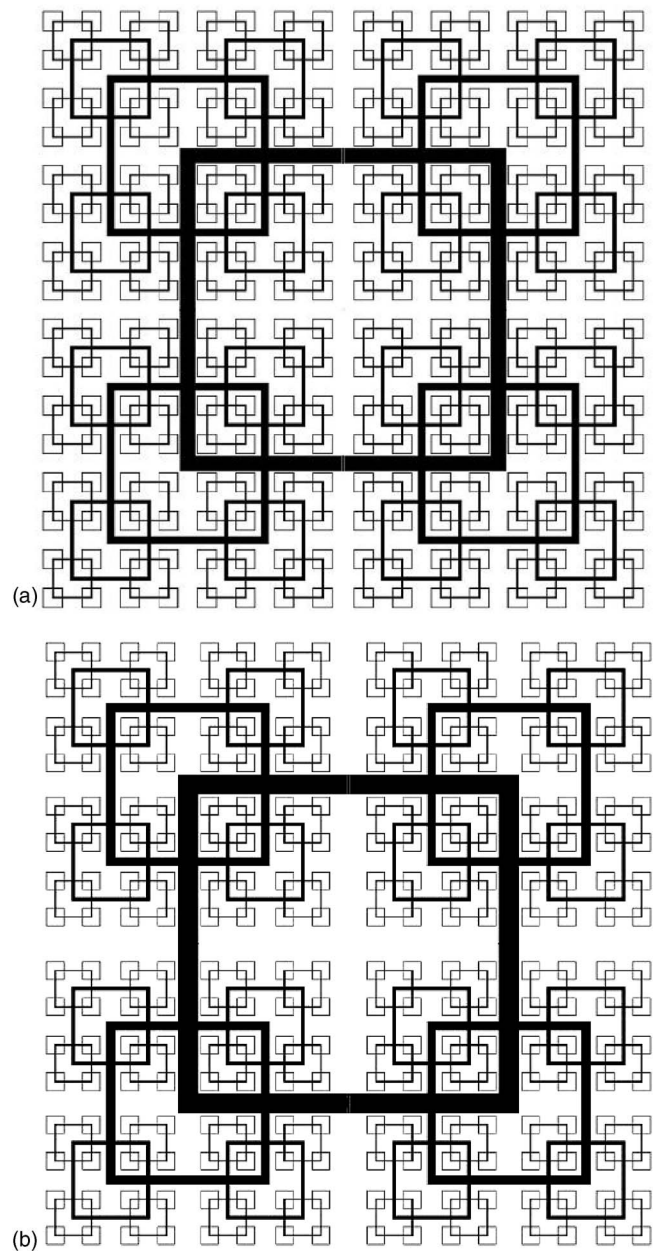


FIG. 33. Scaled diagrams of space-filling square grids for the $T=0.91$ m tunnel: $t_r=17.0$ and 28.0 .

perimeter P of the space-filling square grids in the $T=0.46$ m tunnel is about 39% longer than that of the space-filling I grids in the same tunnel. This is interesting because a longer perimeter should contribute to higher drag via increased viscous blockage.)

$U(x)/U_\infty$ is found to decrease with increasing x at a rate that is faster for larger values of t_r [see $T=0.46$ m tunnel example in Fig. 34(a)]. The flows must therefore be inhomogeneous and have non-negligible turbulence production near the grid. However, turbulence production by $\frac{\partial U}{\partial x}$ falls to levels below 5% of dissipation far enough from the grid for high enough t_r [see the $T=0.46$ m tunnel example in Fig. 34(b), where the production and dissipation are the same forms of \mathcal{P} and ϵ^* used in Fig. 5].

The homogeneity of the U/U_∞ y profiles at our far point

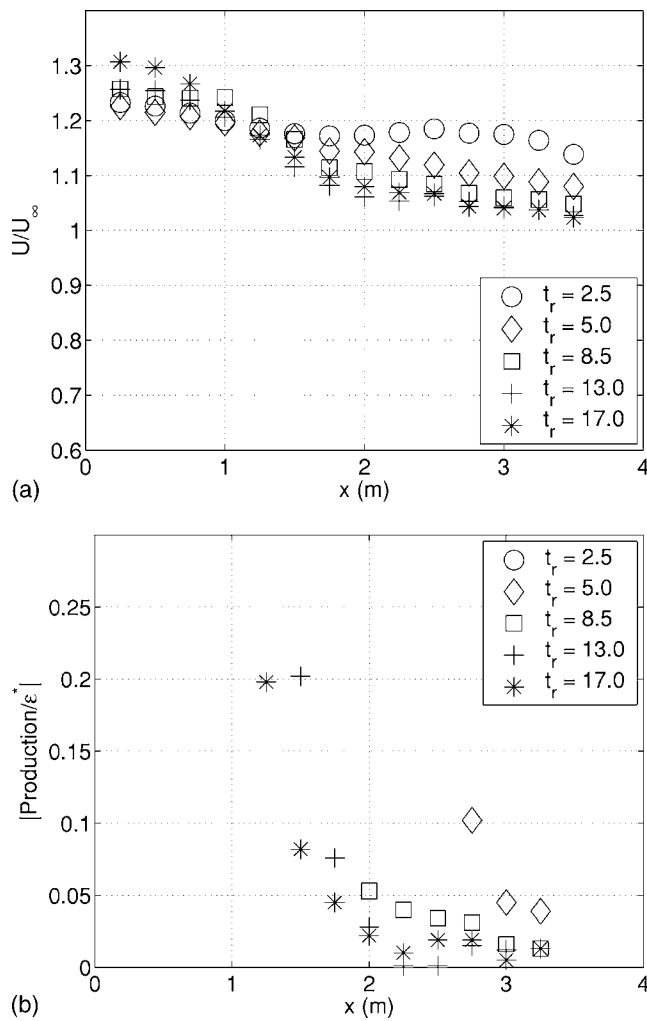


FIG. 34. Turbulence production, space-filling square grids, $T=0.46$ m tunnel, $U_\infty=10$ m/s.

of measurement was found to be good and to improve as t_r increases; similarly, the y profiles of both u'/U and v'/U are satisfactorily homogeneous with the one exception of $t_r=2.5$. In Fig. 35, we plot, as an example, the profiles obtained in the $T=0.46$ m wind tunnel. Lateral and longitudinal integral scales are smaller than 6 cm in all square grid cases (see Fig. 45 in Sec. VI D), and mean profiles are homogeneous across at least five such integral scales. Overall, homogeneity is therefore satisfactory and improves as t_r increases, except close to the grids, where our production and U/U_∞ measurements seem to indicate that the flow is presumably not homogeneous.

It is worth noting, comparing Figs. 35 and 18, that the residual inhomogeneities in the horizontal y direction about the centerline are jet-like in the case of square grids but wake-like in the case of I grids. This clear quantitative difference is most probably correlated with the fact that I grids have a relatively thick vertical bar crossing their center (see Fig. 17), whereas the square grids are characterized by a clear empty strip in that region (see Figs. 32 and 33).

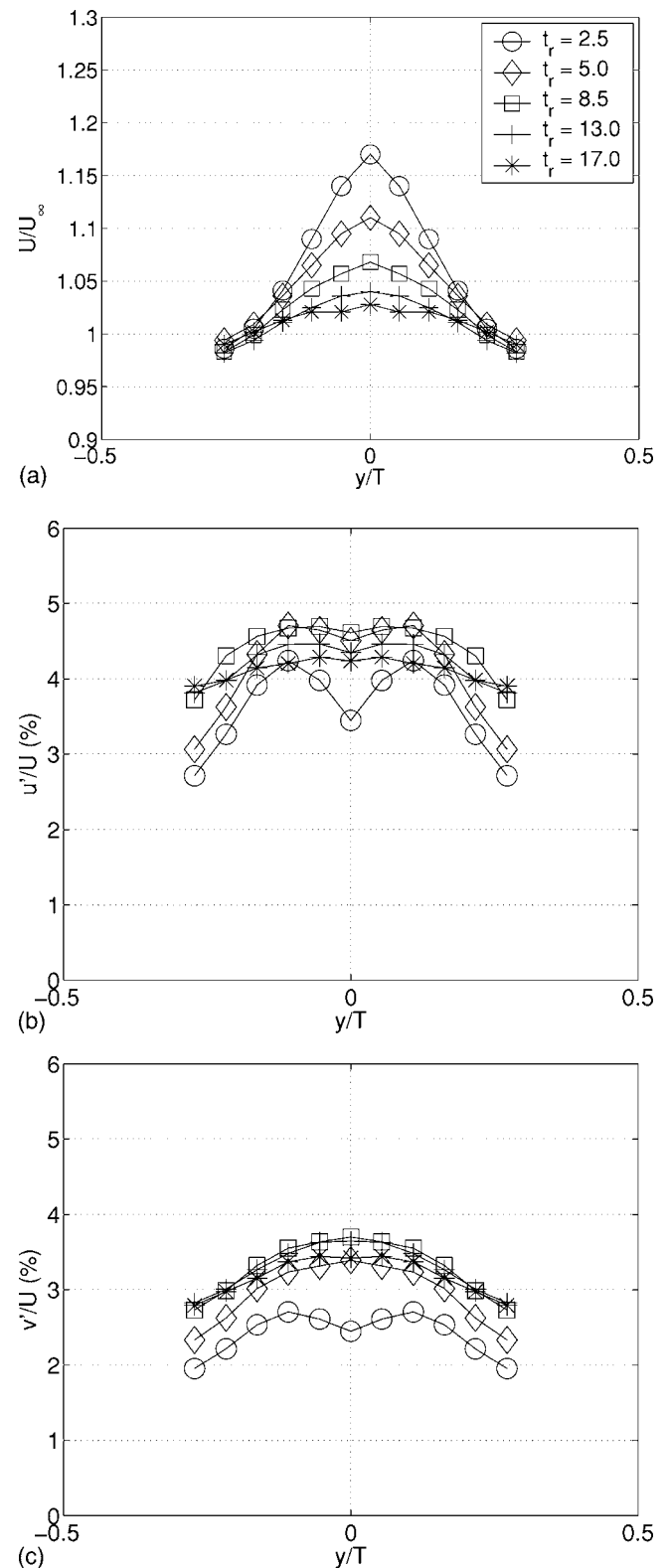


FIG. 35. Homogeneity mean profiles, space-filling square grids, $T=0.46$ m tunnel, $U_\infty=10$ m/s, $x=3.25$ m.

B. Large-scale isotropy

In Fig. 36, we plot u'/v' as a function of x on each tunnel's centerline. We find that u'/v' lies approximately between 1.2 and 1.3 beyond the region close to the grid where $U(x)/U_\infty \geq 1.1$ and for t_r large enough. There is there-

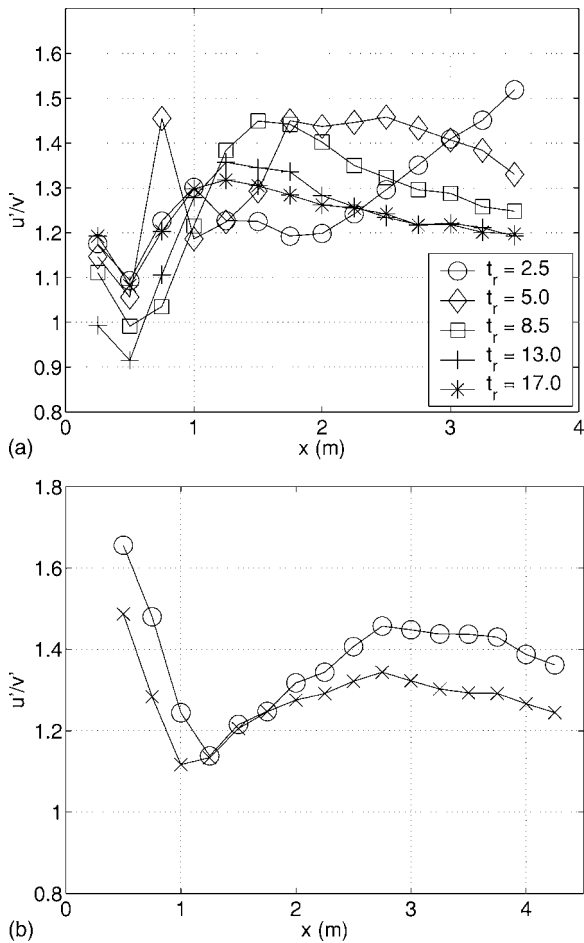


FIG. 36. Large-scale isotropy indicator u'/v' as a function of x (in meters) on the centerline. Space-filling square grids in both tunnels; $U_\infty=10$ m/s for $T=0.46$ m, $U_\infty=12$ m/s for $T=0.91$ m.

fore a distance far enough from the grid where the turbulence isotropy is comparable to that produced by active grids.^{11,12} This conclusion is clear from the results obtained in the $T=0.46$ m tunnel but less so from the $T=0.91$ m tunnel's results. As we are about to see in the following subsection, the length scale which measures how far the turbulence is from

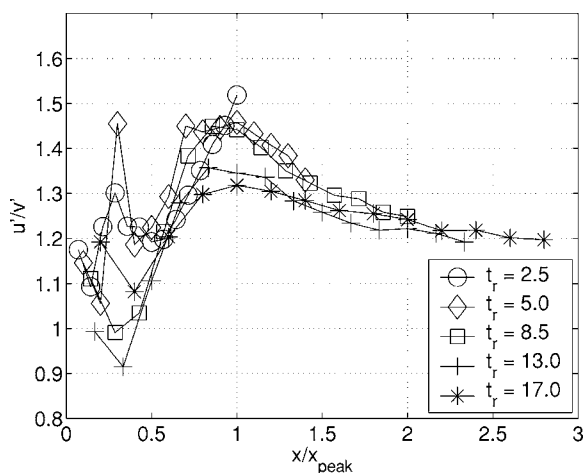


FIG. 37. Large-scale isotropy indicator u'/v' as a function of x/x_{peak} along the centerline. Space-filling square grids; $U_\infty=10$ m/s, $T=0.46$ m tunnel.

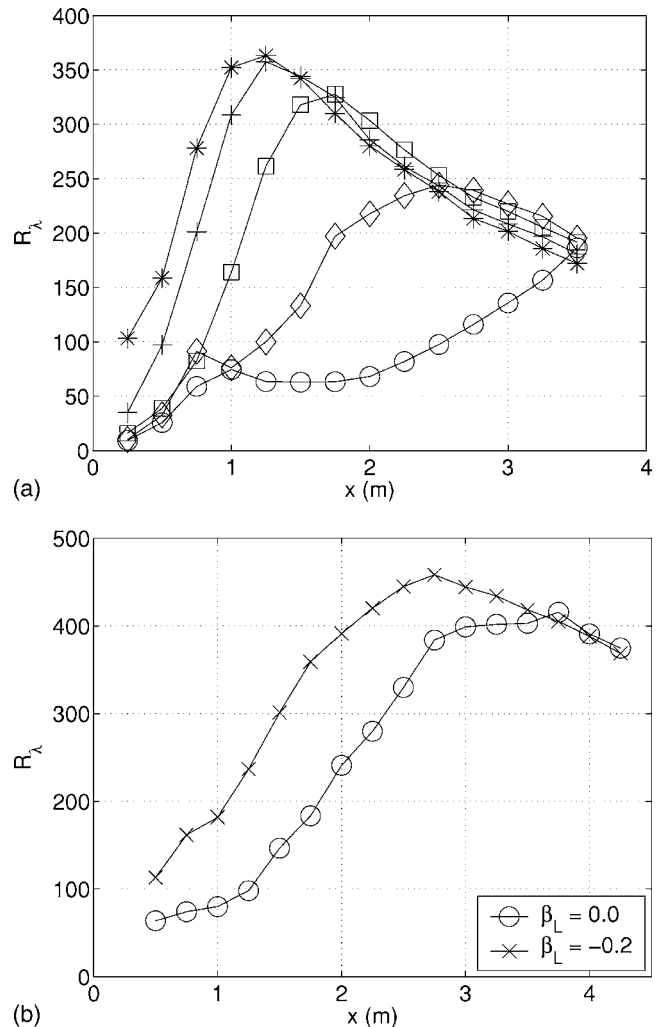


FIG. 38. Re_λ as a function of x measured in meters from the space-filling grids. (a) $U_\infty=10$ m/s in the $T=0.46$ m tunnel and (b) $U_\infty=12$ m/s in the $T=0.91$ m tunnel.

the grid seems to be $x_{peak}=75(t_{min}T/L_{min})$. In the space-filling fractal square grids that we have used here, t_r increases as t_{min} decreases, and therefore the two requirements for acceptable large-scale isotropy, i.e., that x should be large enough and that t_r should also be large enough, are one and the same considering that x is large enough when $x > x_{peak}$. In fact, the u'/v' data of Fig. 36(a) collapse quite nicely when plotted against x/x_{peak} , as can be clearly seen in Fig. 37. This plot shows how u'/v' decreases, in this case apparently toward 1.2, as x increases above x_{peak} .

C. Turbulence decay

In Fig. 38, we plot the decay along the centerline of the Reynolds number Re_λ defined in Sec. IV C for all our square grids in both tunnels. There appears to be a trend not dissimilar to that of space-filling I grids whereby space-filling square grids with higher t_r generate higher Reynolds numbers. In fact, the Reynolds number peaks at higher values but also closer to the grid for higher t_r . The Reynolds numbers generated by the square grids are not as high as those generated by I grids, but are nevertheless higher than Reynolds

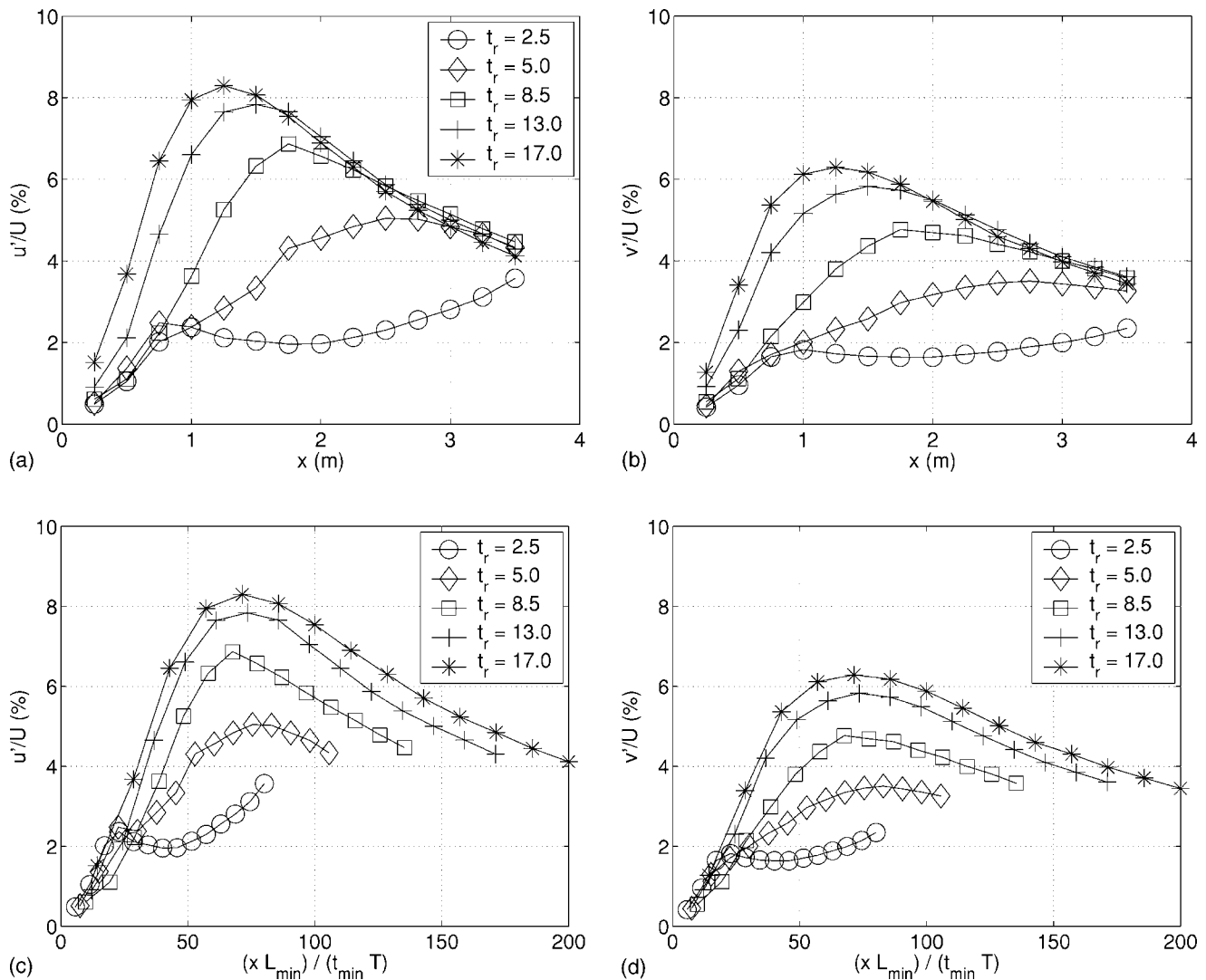


FIG. 39. Turbulence intensities as functions of x in meters and of x/x_{peak} . Space-filling square grids, $T=0.46$ m tunnel, $U_{\infty}=10$ m/s.

numbers generated by classical and cross grids (comparisons at equal blockage ratios). However, the turbulence produced by the I grids is significantly less homogeneous and more anisotropic than the turbulence produced by classical and cross grids and even by square grids if the comparison is made far enough from the grid.

In Fig. 39 we plot, for the five space-filling fractal square grids designed to fit in the $T=0.46$ m tunnel, the development of the turbulent intensities u'/U and v'/U on the centerline as the turbulence is convected downstream. The behavior is identical to that of Re_{λ} : the turbulence intensities build up until they reach a point x_{peak} , where they peak and then decay beyond that point. More striking, perhaps, is the existence of a universal asymptotic decay curve common to all space-filling fractal square grids. The turbulence intensities produced by all these grids meet and follow that decay curve, albeit further downstream for lower values of t_r .

Equally striking are the plots of the turbulence intensities as functions of x/x_{peak} , where

$$x_{\text{peak}} = 75 \frac{t_{\min} T}{L_{\min}}. \quad (6)$$

This result implies that the smallest length scales on the grid determine the distance downstream where the turbulence peaks. The reason for this unusual property may have something to do with the fact that the smallest bars are also the most numerous on the grids. The dependencies of x_{peak} on T and L_{\min} in Eq. (6) have been obtained from comparative analysis of the turbulence intensities in both wind tunnels. Figure 40 is similar to Fig. 39 but for the two space-filling fractal square grids designed to fit in the $T=0.91$ m tunnel. The best fit that we found for x_{peak} taking account of the data in both tunnels is given by Eq. (6).

D. Exponential turbulence decay beyond x_{peak}

It is clear from Fig. 40 that the $T=0.91$ m tunnel's test section is too short in terms of multiples of T for a study of the decay of fractal square grid-generated turbulence beyond

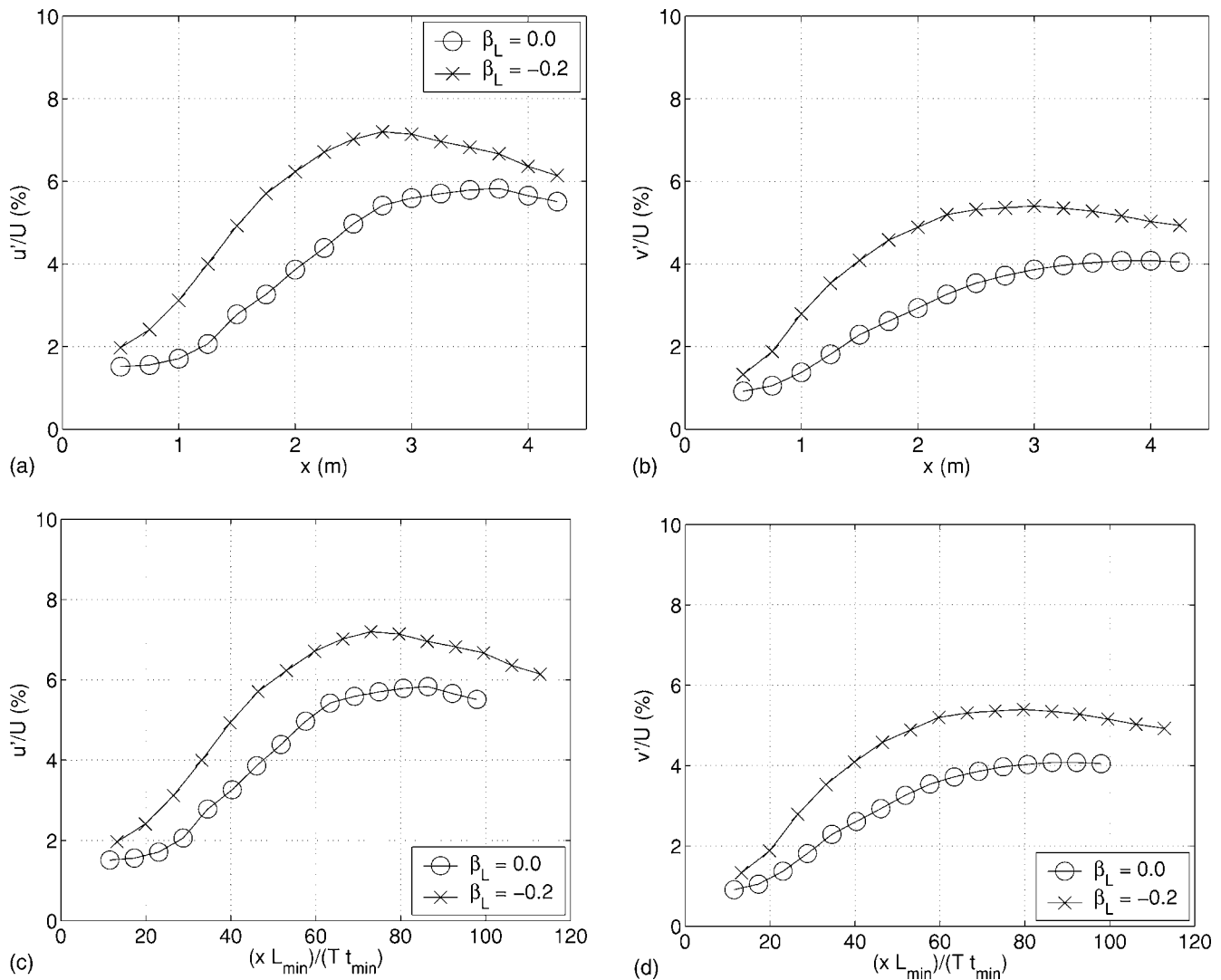


FIG. 40. Turbulence intensities as functions of x in meters and of x/x_{peak} . Space-filling square grids, $T=0.91$ m tunnel, $U_{\infty}=12$ m/s.

x_{peak} . Hence we concentrate on our measurements of turbulence generated by the five square grids in the smaller $T=0.46$ m tunnel for our study of turbulence decay beyond x_{peak} .

As explained in Sec. IV D and under the assumptions stated there, a power-law turbulence decay $u'^2 \sim (x-x_0)^{-n}$ is only possible if $\lambda^2 \sim [\nu(x-x_0)]/U$. Of these assumptions, the Taylor hypothesis can be applied to all our square grid-generated flows as turbulence intensities are small enough in all our points of measurement. Turbulence production and large-scale anisotropy may only be considered small far enough from the grid and for high enough values of t_r (see Figs. 34, 36, and 37). One suspects that the production by $\frac{\partial U}{\partial x}$, like the large-scale anisotropy, drops down to relatively small values at $x \gg x_{\text{peak}}$. Hence, it makes some sense to expect $\lambda^2 \sim \nu(x-x_0)/U$ at $x \gg x_{\text{peak}}$.

In Fig. 41, we plot λ [in millimeters and calculated by direct application of the definition $\lambda^2 \equiv u'^2 / \langle (\frac{1}{U} \frac{\partial u}{\partial x})^2 \rangle$ given in Sec. IV C] as a function of x (in meters) and as a function of x/x_{peak} for the five fractal square grids shown in Fig. 32. The

λ data collapse when plotted against x/x_{peak} . More intriguingly, Fig. 41 suggests that, for $x \gg x_{\text{peak}}$, λ is independent of t_r (it is about the same for all five space-filling square grids) and even approximately independent of x . During turbulence decay far from the fractal square grid where the turbulence seems approximately homogeneous, isotropic, and without turbulence production, the Taylor microscale seems to remain constant. For a double check on this very unusual result, we also calculate $\lambda^* = 15\nu u'^2 / \epsilon^*$ with ϵ^* calculated as for Fig. 5, but only where x_{peak} is sufficiently small to allow measurements at enough values of x sufficiently larger than x_{peak} , i.e., for $t_r=8.5, 13.0, 17.0$ (see Fig. 41, where we also add three data points for $t_r=5.0$). These measurements of λ^* confirm the constancy of the Taylor microscale during turbulence decay at distances $x \gg x_{\text{peak}}$, and measurements of λ in the $T=0.91$ m tunnel confirm this too (see Fig. 42).

To determine whether the Taylor microscale can indeed be considered constant during turbulence decay or whether it can instead be reasonably well fitted by a power law $\lambda \sim (x-x_0)^s$, we apply the procedure of Secs. IV D and V G to the

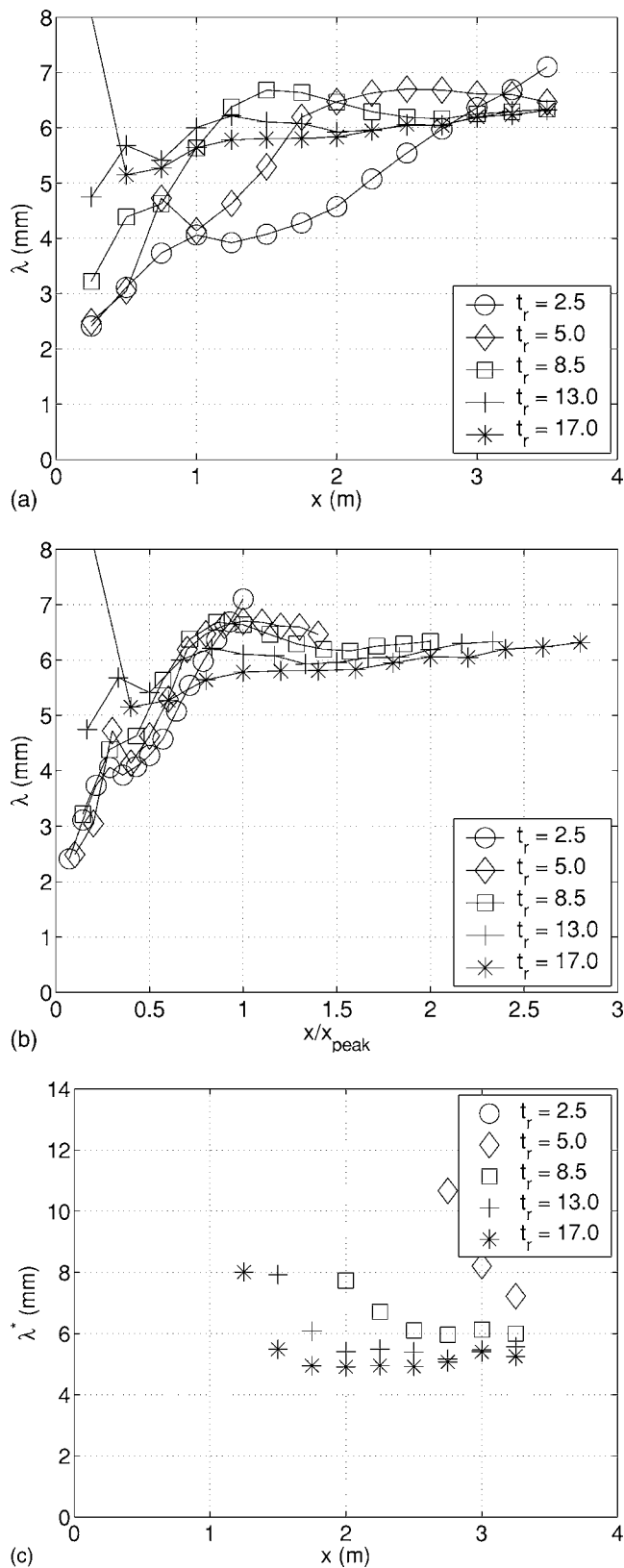


FIG. 41. Taylor microscales λ and λ^* as functions of x (in meters) and x/x_{peak} . Space-filling fractal square grids, $T=0.46$ m tunnel, $U_\infty=10$ m/s.

turbulence generated by the $t_r=17$ fractal square grid because it has the smallest x_{peak} and therefore the longest measurable extent of turbulence decay in the tunnel's test section. For each x_0 , we determine the best-fit values of s and s^*

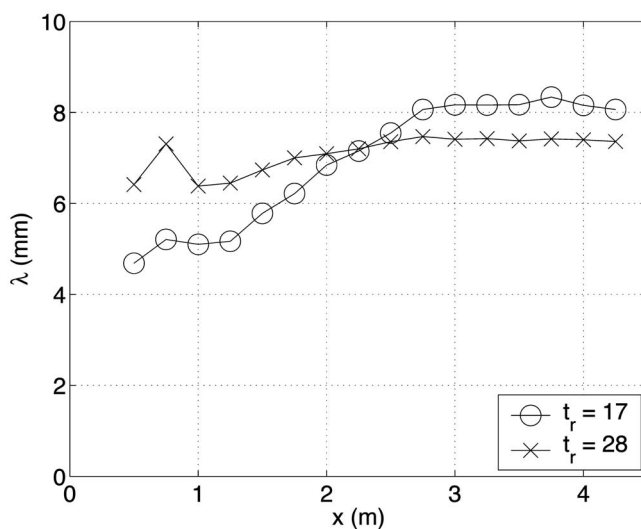


FIG. 42. Taylor microscale λ as a function of x (in meters). Space-filling fractal square grids, $T=0.91$ m tunnel, $U_\infty=12$ m/s. For the $t_r=17$ grid, $x_{peak} \approx 2.75$ m and for the $t_r=28$ grid, $x_{peak} \approx 3.2$ m. In both cases, λ is approximately constant where $x > x_{peak}$.

in $\lambda \sim (x-x_0)^s$ and $\lambda^* \sim (x-x_0)^{s^*}$ and also the best-fit values of n in the assumed power law $u'^2 \sim (x-x_0)^{-n}$. Results are plotted in Figs. 43 and 44. In particular, these results show that $\lambda \sim [\nu(x-x_0)/U]^{0.5}$ requires $x_0 < -8.4$ m. Such very large negative values of x_0 would imply $u'^2 \sim (x-x_0)^{-n}$ with $n > 6.75$, much steeper than any existing theory and measurements would suggest.^{9,14,16-19} If we were to choose $x_0 \approx 0$ just to put ourselves artificially in line with measurements of x_0 obtained from turbulence generated by classical and active grids,^{16,17} we would be led to $1 \leq n \leq 2$, in agreement with previous theories and measurements, but also to $\lambda \approx (x-x_0)^s$, where $s \approx 0.1$, which is incompatible with a power-law turbulence decay.

We are therefore led to conclude, as Fig. 41 suggests, that the Taylor microscale remains, to good first approximation, constant during turbulence decay (there may actually be a slight increase with x , but to a first approximation for the purposes of this paper, we consider λ to be constant, particularly because this very slight increase cannot be accounted for by the usual power-law fits). Specifically, $\lambda \approx 6$ mm at all $x \gg x_{peak}$ for all our space-filling square grids in the $T=0.46$ m tunnel with $U_\infty=10$ m/s. (We find λ between 7 and 8 mm in the $T=0.91$ m tunnel with $U_\infty=12$ m/s. This tunnel has a shorter test section in multiples of T , which means that we cannot measure much beyond x_{peak} in it.)

The principle of permanence of large eddies applied to isotropic homogeneous turbulence implies¹⁸ that a low wave-number energy spectrum of the form $E_{11}(k_1) \sim k_1^q$ leads to $u'^2 \sim (x-x_0)^{-n}$ and integral scale $L_u \sim (x-x_0)^m$ with $n=2(1-m)$ and $n=2(1+q)/(3+q)$. Our space-filling square grids produce integral scales that remain approximately constant during decay at $x \gg x_{peak}$, i.e., $m \approx 0$ (see Fig. 45). Values of m very close to 0 would imply $n \approx 2$ and $q \rightarrow \infty$. The validity of the principle of permanence of large eddies is doubtful for $q \geq 4$ as noted, for example, by Frisch,¹⁸ and we are therefore led to conclude that it does not apply to the turbulence gen-

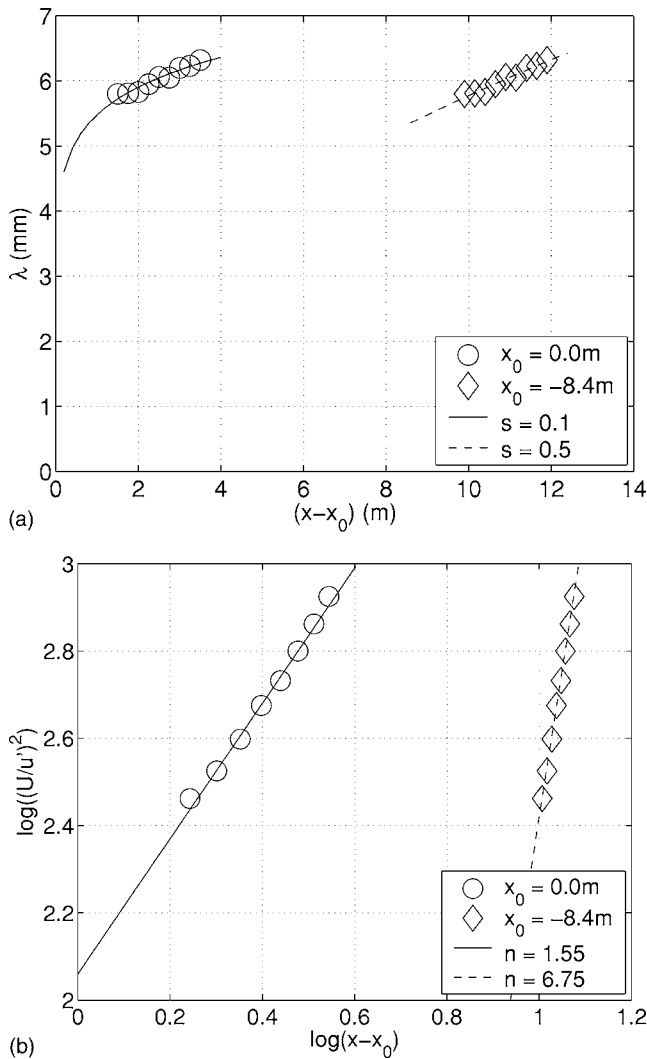


FIG. 43. Taylor microscale λ (in millimeters) as a function of $x-x_0$ (in meters) and $\log(U/u')^2$ as a function of $\log(x-x_0)$ for two values of x_0 with power-law best-fit curves through data. The best-fit values of s and n for each x_0 are given in the plots. Space-filling fractal square grid $t_r=17$, $T=0.46$ m tunnel, $U_\infty=10$ m/s.

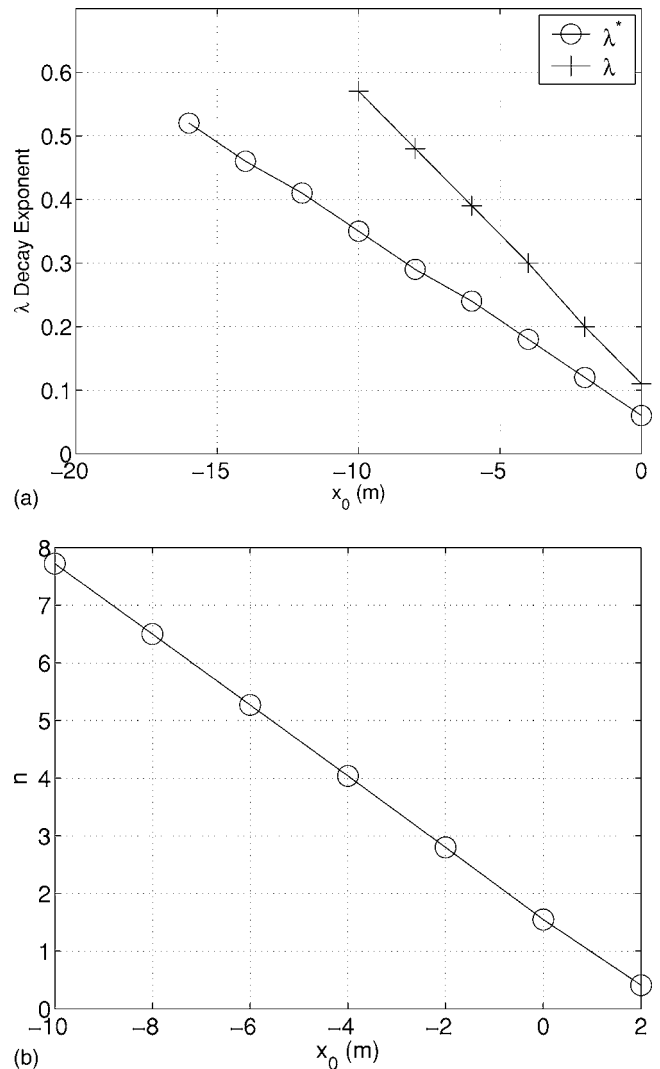


FIG. 44. Exponents s, s^* , and n as functions of x_0 (in meters). Space-filling fractal square grids $t_r=17$, $T=0.46$ m tunnel, $U_\infty=10$ m/s.

erated by our space-filling fractal square grids. In fact, to be precise, at $U_\infty=10$ m/s in the $T=0.46$ m tunnel, for all $x \gg x_{\text{peak}}$ and for all five space-filling square grids, $\lambda \approx 6$ mm, $L_u \approx 48$ mm, and $L_v \approx 22$ mm (about $L_u/2$ as required by isotropy). Note that all these length scales are much smaller (ten times or more) than $T=0.46$ m. It may therefore be difficult to account their constancy in time (i.e., with x) on the finite size of the tunnel's width.

Assuming large- and small-scale isotropy, negligible turbulence production, and Taylor's hypothesis, $-\frac{3}{2}U(du'^2/dx) = 15\nu u'^2/\lambda^2$. Hence, $\lambda = \lambda_0$ independent of x implies

$$u'^2 = u'_{\text{peak}}{}^2 \exp[-(x - x_{\text{peak}})/l_{\text{turb}}], \quad (7)$$

where x_{peak} , given by Eq. (6), is the distance from the grid where the turbulence fully intensifies, and

$$l_{\text{turb}} = 0.1\lambda_0 \frac{U\lambda_0}{\nu} \quad (8)$$

is the distance beyond x_{peak} that the turbulence lasts. This exponential decay law is supported by our measurements both for u'^2 and v'^2 , as evidenced in Fig. 46. Note, by the way, that we find $u'_{\text{peak}}{}^2$ to increase linearly with t_r , and that it is a bit larger than the measured $u'^2(x=x_{\text{peak}})$.

In an unpublished manuscript dating from 2003, George and Wang predicted the possibility of constant length scales during exponential turbulence decay but as a result of eddies having grown so large that they would stop growing because of wall confinement. At first sight, it might be hard to imagine how wall confinement could have an effect in our measurements where T is at least an order of magnitude larger than our measured integral scales. However, fluid mechanical barriers resulting from the interactions between the various elementary flows generated by the various multisized squares of the fractal square grid are not inconceivable, and work in this direction is currently underway by one of the authors of the present paper.

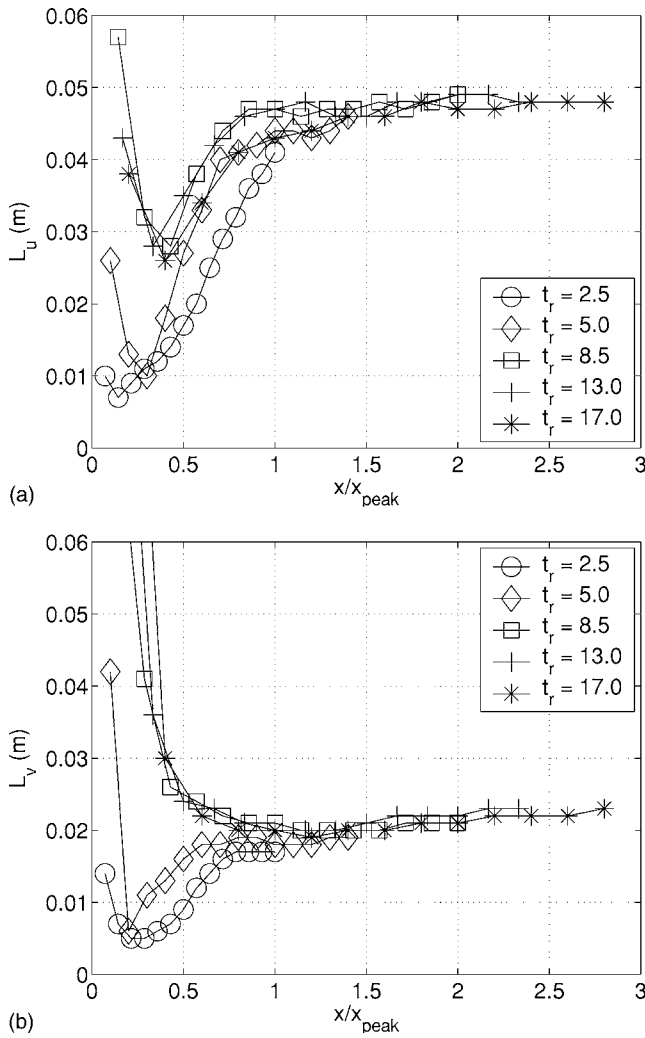


FIG. 45. Longitudinal (L_u) and lateral (L_v) integral scales as functions of x/x_{peak} . Space-filling fractal square grids, $T=0.46$ m tunnel, $U_\infty=10$ m/s.

E. Third conclusions: Space-filling fractal square grids

Our conclusions on the space-filling fractal square grids can be summarized as follows:

- (i) The normalized static pressure drop is nearly independent of t_r (in fact very slowly increasing with increasing t_r).
- (ii) Far enough from the grid (beyond x_{peak}), homogeneity is satisfactory and improves as t_r increases.
- (iii) Turbulence production by $\frac{\partial U}{\partial x}$ falls to levels below 10% of dissipation far enough from the grid and for high enough t_r .
- (iv) Large-scale isotropy: u'/v' lies approximately between 1.2 and 1.3 beyond the region close to the grid where $U(x)/U_\infty \geq 1.1$ and for t_r large enough. u'/v' collapses as a function of x/x_{peak} , where $x_{peak} = 75(t_{min}T/L_{min})$.

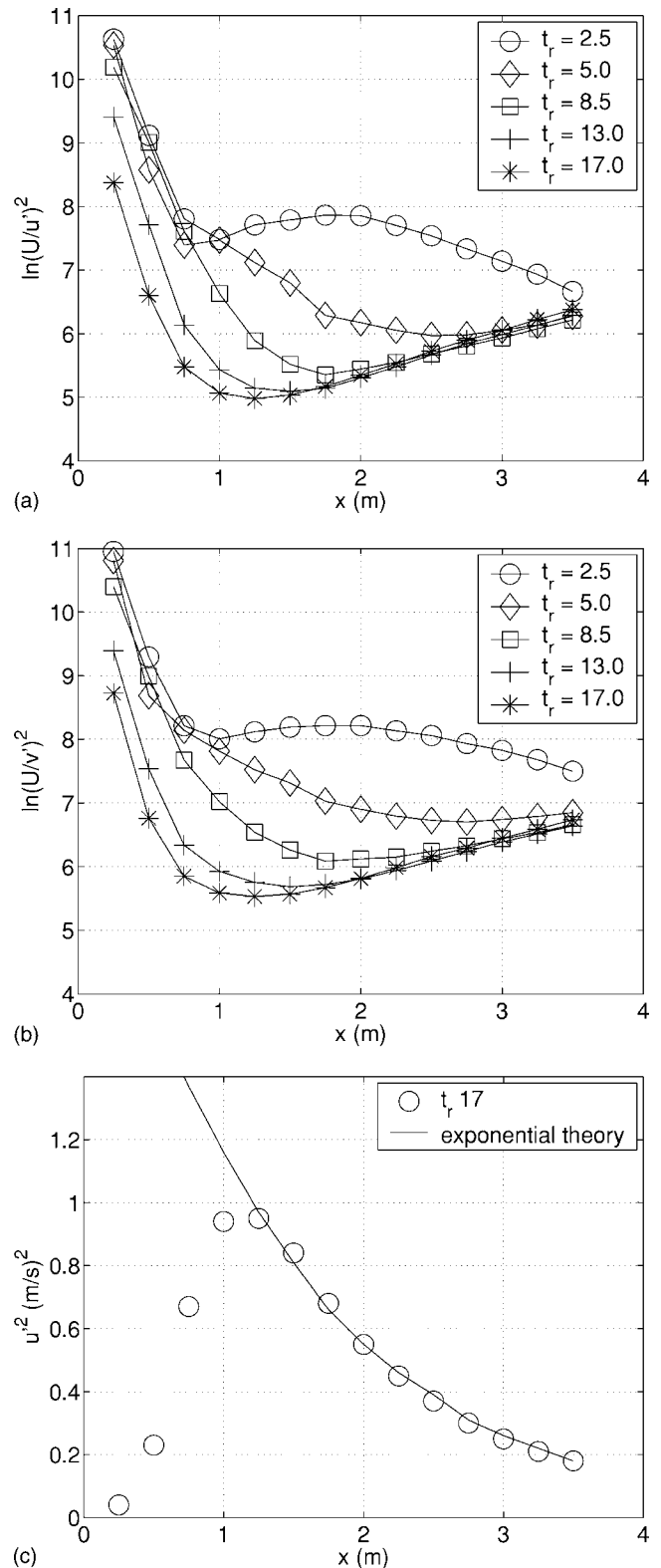


FIG. 46. $T=0.46$ m tunnel with $U_\infty=10$ m/s. (a) $\ln(U/u')^2$ and (b) $\ln(U/v')^2$ as functions of x (in meters) for all five space-filling fractal square grids revealing the straight line [in agreement with Eq. (7)] on which the turbulence decay curves generated by all these grids eventually asymptote to. (c) u'^2 in m^2/s^2 as a function of x in meters with exponential fit according to Eq. (7) for $t_r=17$.

- (v) The principle of permanence of large eddies does not hold and the turbulence decay seems to be exponential for $x \gg x_{peak}$. Specifically, $u'^2 = u'_{peak}{}^2 \exp[-(x - x_{peak})/l_{turb}]$, where $u'_{peak}{}^2$ increases linearly with t_r ,

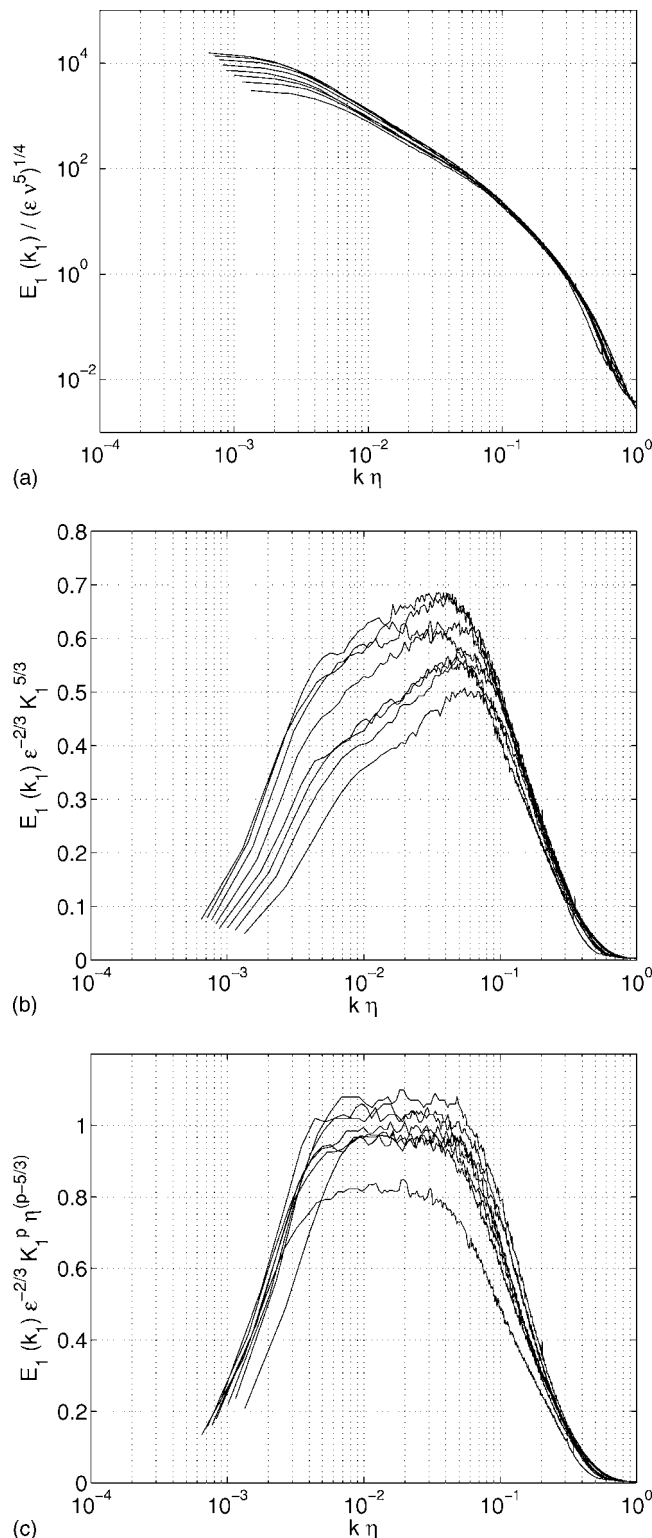


FIG. 47. Energy spectra at $x=3.25$ m downstream the $t_r=13$ fractal square grid in the $T=0.46$ m tunnel at eight different speeds U_z ranging between 6 and 20 m/s in 2 m/s increments.

$l_{\text{turb}}=0.1\lambda \frac{L\lambda}{\nu}$, and λ is the Taylor microscale, which appears to remain approximately constant during turbulence decay beyond x_{peak} . The integral length scales also remain constant during decay beyond x_{peak} and they are independent of t_r , as is λ .

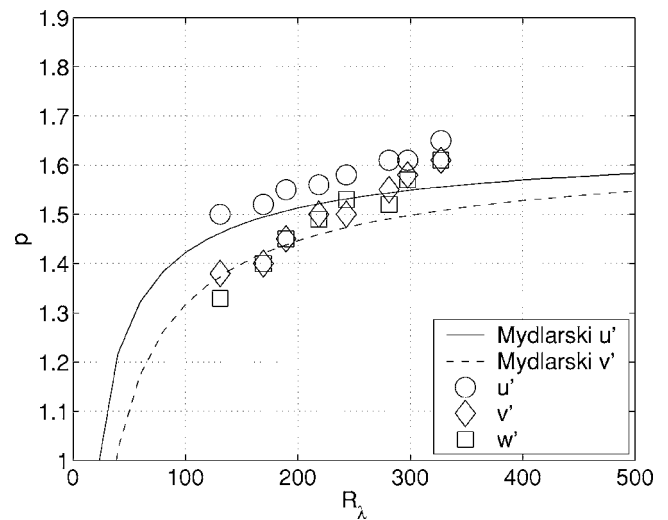


FIG. 48. Exponents p of power-law energy spectra (see third plot of previous figure) as functions of Re_λ at $x=3.25$ m downstream the $t_r=13$ fractal square grid in the $T=0.46$ m tunnel. The lines marked “Mydlarski” are best fits obtained by Mydlarski and Warhaft (Ref. 12) for the Re_λ dependence of the exponents p in the power law u and v spectra obtained in active grid-generated turbulence.

VII. OVERALL CONCLUSIONS

D_f , t_r , and M_{eff} are important fractal grid parameters. Best homogeneity is obtained for $D_f=2$. For space-filling fractal I and square grids, homogeneity can be further improved by increasing t_r . In all cases of fractal grids, turbulence intensity and Reynolds number can also be increased by increasing t_r . However, high values of t_r can lead, at least in the case of space-filling fractal I grids, to increased turbulence production by $\frac{\partial U}{\partial x}$. In the case of space-filling square grids, they lead to a muting of turbulence production far enough from the grid. In that case, $t_{\text{min}}/L_{\text{min}}$ is also an important parameter.

Not only the large scales, but all anisotropic scales of fractal grids are potentially responsible for the large-scale turbulence anisotropy that these grids might generate. At the very least, there is compelling evidence to this effect in the case of fractal I grids.

The scalings and decay of the turbulence intensities along the x direction on the tunnel’s centerline are as follows:

- (i) For fractal cross grids ($D_f=2$), both $(u'/U)^2$ and $(v'/U)^2$ are well collapsed by $t_r^2 C_{\Delta P} fct(x/M_{\text{eff}})$.
- (ii) For fractal I grids, $(u'/U)^2 = t_r(T/L_{\text{max}})^2 C_{\Delta P} fct(x/M_{\text{eff}})$ [and similarly for $(v'/U)^2$ and $(w'/U)^2$], where T is the tunnel width and L_{max} is the maximum bar length on the grid.
- (iii) For space-filling ($D_f=2$) fractal square grids, the turbulence intensity builds up as the turbulence is convected downstream until a distance x_{peak} from the grid is reached where the turbulence intensity peaks and then decays exponentially, $u'^2 = u'_{\text{peak}}{}^2 \exp[-(x - x_{\text{peak}})/l_{\text{turb}}]$, where $u'_{\text{peak}}{}^2$ increases linearly with t_r , $x_{\text{peak}} \propto t_{\text{min}} T/L_{\text{min}}$ (L_{min} being the minimum bar thickness on the grid), and $l_{\text{turb}} \propto \lambda^2 U/\nu$, ν being the kine-

matic viscosity of the air and λ being the Taylor microscale, which remains approximately constant during decay at $x \gg x_{\text{peak}}$. The longitudinal and lateral integral length scales also remain approximately constant during decay at $x \gg x_{\text{peak}}$.

Clearly, these results call for many more measurements to be made in wind tunnel turbulence generated by fractal grids. Mean velocity and turbulence intensity profiles need to be collected in many more stations than has been possible in the present exploratory work. The decay of turbulence intensities needs to be measured off center-axis for completeness and interpretation purposes. Mixing studies and applications should be considered; the prospect of increasing turbulence intensities by increasing parameters such as t_r and T/L_{max} without increasing pressure drop points at possibilities for energy efficient mixing. Also, it will be interesting to see whether scalar variances in fractal-generated turbulence scale and decay similarly to turbulence intensities. Relations such as (3)–(8) open up the possibility of what may be termed *multiscale flow control*, which in the case of fractal grids is passive. It seems possible, for example, to control the distance x_{peak} downstream of a fractal square grid where the turbulence builds up by controlling the smallest thickness t_{min} on the grid. It also seems possible to control the turbulence intensity by controlling t_r , the ratio of maximum to minimum thicknesses, in different ways for all three families of fractal grids presented here. Distances downstream can be meaningfully measured in terms of the effective mesh size M_{eff} , which we have introduced in this paper, and in the case of fractal square grids, the distance l_{turb} after buildup over which the turbulence lasts may also be controlled.

Finally, two-point statistics such as energy spectra need to be calculated at various stations in the wind tunnel, in particular to assist with the interpretation of the apparent exponential turbulence decay far downstream of fractal square grids. Equally important are coherence spectra $C(k_1) \equiv |E_{12}(k_1)|^2 / E_{11}(k_1)E_{22}(k_1)$, which measure tendencies toward or away from small-scale isotropy. Indeed, in this paper we have often taken kinetic energy dissipation rate per unit mass to equal $15\nu u'^2/\lambda^2$, which assumes small-scale isotropy, and our conclusion that the turbulence far downstream of fractal square grids decays exponentially relies on this relation [in fact, on the proportionality $-\frac{3}{2}U(du'^2/dx) \sim \nu u'^2/\lambda^2$, not on the specific value of the constant of proportionality]. Comprehensive and careful studies of coherence spectra of turbulence generated by fractal grids need to be carried out.

Preempting future publications, we close this paper with examples of spectral results collected at $x=3.25$ m downstream of the $t_r=13$ fractal square grid in the $T=0.46$ m tunnel at eight different speeds U_∞ ranging between 6 and

20 m/s in 2 m/s increments. Figures 47 and 48 show that the energy spectra are broad and continuous and well approximated by power-law dependencies on wave number with exponents $-p$, which seem to tend toward the Kolmogorov value $-5/3$ as Re_λ increases. We are currently working on how such spectra can account for exponential turbulence decay laws and for integral and Taylor length scales that remain constant during decay. Coherence spectra are an integral part of this forthcoming study.

ACKNOWLEDGMENTS

We are grateful to Dr. Mike Kearney of Amalgamated Research Inc. for his cooperation with the construction of the I and square fractal grids, to Dr. N. Mazellier for help with classical grid measurements and very useful discussions, and to Professor W. K. George for bringing to our attention his paper with Han and Hjarne.¹³

- ¹D. Queiros-Conde and J. C. Vassilicos, "Turbulent wakes of 3D fractal grids," in *Intermittency in Turbulent Flows*, edited by J. C. Vassilicos (Cambridge University Press, Cambridge, 2001).
- ²B. Mazzi, F. Okkels, and J. C. Vassilicos, "A shell model approach to fractal induced turbulence," *Eur. Phys. J. B* **28**, 243 (2002).
- ³A. Staicu, B. Mazzi, J. C. Vassilicos, and W. van der Water, "Turbulent wakes of fractal objects," *Phys. Rev. E* **67**, 066306 (2003).
- ⁴B. Mazzi and J. C. Vassilicos, "Fractal-generated turbulence," *J. Fluid Mech.* **502**, 65 (2004).
- ⁵L. Biferale, M. Cencini, A. S. Lanotte, M. Sbragaglia, and F. Toschi, "Anomalous scaling and universality in hydrodynamic systems with power-law forcing," *New J. Phys.* **6**, 37 (2004).
- ⁶L. Biferale, A. S. Lanotte, and F. Toschi, "Effects of forcing in three-dimensional turbulence," *Phys. Rev. Lett.* **92**, 094503 (2004).
- ⁷A. K. Kuczaj, B. J. Geurts, and W. D. McComb, "Nonlocal modulation of the energy cascade in broadband-forced turbulence," *Phys. Rev. E* **74**, 016306 (2006).
- ⁸G. K. Batchelor, *The Theory of Homogeneous Turbulence* (Cambridge University Press, Cambridge, 1953).
- ⁹S. Corrsin, "Turbulence: Experimental methods," in *Handbook der Physik* (Springer, New York, 1963), p. 524.
- ¹⁰G. Comte-Bellot and S. Corrsin, "The use of a contraction to improve the isotropy of grid-generated turbulence," *J. Fluid Mech.* **25**, 657 (1966).
- ¹¹H. Makita, "Realization of a large-scale turbulence field in a small wind tunnel," *Fluid Dyn. Res.* **8**, 53 (1991).
- ¹²L. Mydlarski and Z. Warhaft, "On the onset of high-Reynolds-number grid-generated wind tunnel turbulence," *J. Fluid Mech.* **320**, 331 (1996).
- ¹³Y. O. Han, W. K. George, and J. Hjarne, "Effect of a contraction on turbulence. Part 1: Experiment," AIAA-2005-1119, 43d AIAA Aerospace Science Meeting and Exhibit, Reno, NV (2005).
- ¹⁴G. K. Batchelor and A. A. Townsend, "Decay of isotropic turbulence in the initial period," *Proc. R. Soc. London, Ser. A* **193**, 539 (1948).
- ¹⁵G. I. Taylor, "Statistical theory of turbulence," *Proc. R. Soc. London, Ser. A* **151**, 421 (1935).
- ¹⁶M. S. Mohamed and J. C. LaRue, "The decay power law in grid-generated turbulence," *J. Fluid Mech.* **219**, 195 (1990).
- ¹⁷H. S. Kang, S. Chester, and C. Meneveau, "Decaying turbulence in active-grid-generated flow and comparisons with large-eddy simulations," *J. Fluid Mech.* **480**, 129 (2003).
- ¹⁸U. Frisch, *Turbulence: The Legacy of A. N. Kolmogorov* (Cambridge University Press, Cambridge, 1995).
- ¹⁹W. K. George, "The decay of homogeneous turbulence," *Phys. Fluids A* **4**, 1492 (1992).